DESIGN OF A MICROSTRIP ANTENNA AND PCB FOR USE IN AN ELECTROCORTICOGRAPHY BIOMEDICAL IMPLANT

by

Jakob Ian Xiaohou West

A thesis submitted to the faculty of
The University of North Carolina at Charlotte
in partial fulfillment of the requirements
for the degree of Master of Science in
Electrical Engineering

Charlotte

2019

Approved by:

Dr. Ryan Adams

Dr. Thomas Weldon

Dr. Kathryn Smith

ABSTRACT

JAKOB IAN XIAOHOU WEST. Design of a Microstrip Antenna and PCB for use in an Electrocorticography Biomedical Implant. (Under the direction of DR. RYAN ADAMS)

An implantable system, that is part of a wireless body area network, is under development for a study monitoring of neural activity in rats with epilepsy. The study will continue over a nine month period to collect data for epilepsy research. This implantable system is part of a wireless body area network (WBAN) that consists of the implant, a data link, and a base station. The implant contains an insulation layer, an antenna, electronic components, and a power supply. A grid of electrodes implanted into the rat will serve to relay brain signals through the electronics to the antenna. A microstrip antenna is designed to operate in the unlicensed 2.4GHz ISM band to facilitate the wireless data link in the WBAN. Because the implanted system is surrounded by conductive biological tissue, it must be encapsulated in an insulating layer that shields the subject and the implant from each other. The dielectric properties of these tissues are modeled over time and frequency by a Cole-Cole model that is used in simulation software. The specific absorption rate (SAR) of these tissues is investigated, with respect to the input power of the antenna, to determine if the implant is safe to be used on a live subject. The communication system that captures the brain signals and digitizes them to be sent wirelessly over the data link for analysis at the base station is designed with off the shelf components.

DEDICATION

This thesis is dedicated to all my friends who always knew that I was capable of more than I ever thought I was.

ACKNOWLEDGEMENTS

I would like to thank Dr. Ryan Adams for providing me with invaluable knowledge and guidance. I would also like to thank Stephanie LaClair who, even after office hours, was always willing to help me.

TABLE OF CONTENTS

LIST OF TABLES

LIST OF FIGURES

LIST OF ABBREVIATIONS

ADC	Analog to digital converter
cEEG	Continuous electroencephalogram
DUT	Device under test
EIRP	Effective isotropic radiated power
EM	Electromagnetic
ESA	Electrically Small Antenna
FCC	Federal Communications Commission
FF	Far field
FNBW	First null beamwidth
HFSS	High Frequency Structure Simulator
HPBW	Half-power beamwidth
ILAE	International League Against Epilepsy
ISM	Industrial Scientific Medical
NF	Near field
PEC	Perfect electric conductor
PIFA	Planar inverted F antenna
PMC	Perfect magnetic conductor
Rf	Radio frequency
SAR	Specific Absorption Rate
WBAN	Wireless body area network

CHAPTER 1: INTRODUCTION

In 1895 it was first discovered that X-ray radiation could be used to create medical photographs. Since then, electromagnetic (EM) radiation has been continuously investigated in the field of medicine. New applications such as ingestible bio-capsules [5], wireless pacemakers [6], implantable antennas [7], etc. have all been possible due to the increasing research. The advent of EM and radio-frequency (RF) engineering in the medical field has allowed for better understanding of disease prevention and diagnosis [8]. One particular disease that needs more research, which can be aided by an implantable EM device, is epilepsy.

Epilepsy is one of the most common neurological disease affecting approximately 50 million people worldwide. The detection and treatment of neurological diseases has been enhanced by signal and image processing technologies such as EEG (electroencephalogram), CT (computed tomography), MRI (magnetic resonance imaging), and PET (positron emission tomography) [9]. During an iEEG (implanted EEG), signals are recorded from electrodes placed on the brain and analyzed. This is typically done with a physical connection where the wires are connected to the electrodes and the data recording machine; although, advancements in RF allow for this to be replaced with a wireless system so that the patient can be free from the machine. Wireless capture of the electrical signals from the brain could be achieved with an implantable antenna connected to the electrodes. An implantable antenna system can be viewed as part of a wireless body area network (WBAN) and a sample WBAN is shown in figure 1.1.

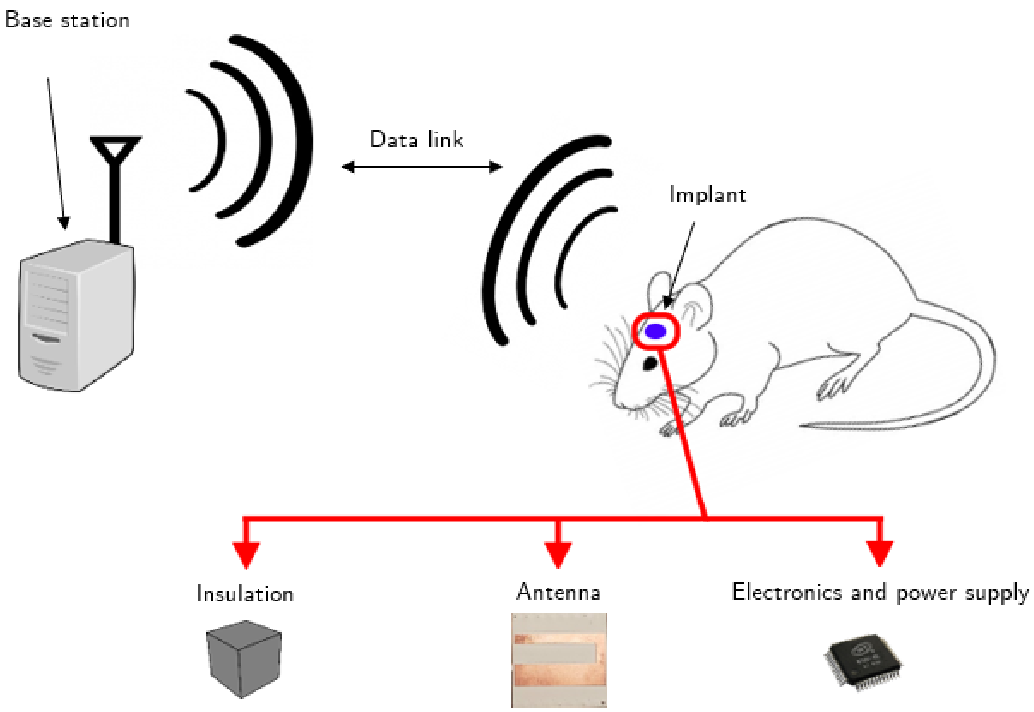

Figure 1.1: Sample WBAN including the implant and base station with data link.

A WBAN typically consists of an implanted device that wirelessly communicates with a base station where the data can be sent to a system for interpretation. This thesis deals with the design and simulation of a wireless implant for use with an iEEG system that will interface with a rat. The implant will remain in the rat over an extended period of time and wirelessly transmit iEEG data to a base station.

1.1 Notable Aspects of a Wireless Implant System for Data Telemetry

The goal of an implantable antenna is to provide a reliable wireless link to an external base station for telemetry. Besides the antenna and the base station the system includes insulation, electronics, and a power supply. Each stage must be designed or carefully selected in order to maximize performance, as well as bio-compatibility.

The base station includes a receiving module, including an antenna, and a system for data storage and transfer. The characteristics of the receiver (such as sensitivity, gain, efficiency, and polarization) must be accounted for or designed for a properly functioning system.

Insulators in the system are added for bio-compatibility as well as shielding the electronic components from the body. Tissues in the body will need to be characterized and understood to design an implant. It will be shown that adding an insulating layer will enhance the operation of the implanted antenna.

The electronics will interface directly with the designed antenna and will be responsible for signal conditioning. These electronics will compose a traditional RF front end which typically includes analog to digital converters (ADC), amplifiers, mixers, etc. These can be off-the-shelf components or custom made components.

The power supply in this system will be assumed to be from [10]. This system, designed by Stuemke, is a closed loop wireless power transfer circuit that can provide power from distances of 1cm to 25cm.

1.2 Frequency Bands

Frequency band characteristics include operating frequencies, data rate, and power limits. The frequency band of interest for this thesis is the 2.4GHz industrial, scientific, and medical (ISM) band. Although, this is an unlicensed band, there are still emissions standards that devices must adhere to. Since there are many ways to quantify the emissions from a device there is a standard measurement used by the federal communication commission (FCC) known as effective isotropic radiated power (EIRP). It is defined as

$$\text{EIRP} = 10\log\left(\frac{E^2 \times r^2}{0.030[V^2]}\right) \tag{1.1}$$

where E is the electric field strength, measured at a distance r, and V is the unit of volts. Measuring the E field strength alone is a precise value and metric, but from a design perspective it may not be as useful as EIRP. The EIRP is the power that would be necessary to provide to an ideal antenna, that radiates in all directions equally, that would produce the same field strength as the device under test (DUT). The ideal antenna that was just described is known as an isotropic radiator.

The FCC defines three types of radiators: intentional, unintentional, and incidental. An intentional radiator is one that is specifically designed to radiate RF power, such as an antenna. Devices like receivers with an attached local oscillator (LO) are designed to operate with RF power, but not radiate, defining an unintentional radiator. Incidental radiators are those devices that are not designed to generate RF power at all, such as a DC motor, but may radiate them unintentionally. Allowable emissions are defined for radiators and they are summarized in table 1.1 for the 2.4GHz ISM band.

Table 1.1: FCC Limits for the 2.4GHz ISM band [1]

	Fundamental		**Harmonics**	
Transmission Type	E at 3m	EIRP	E at 3m	EIRP
Digitally Spread		+36dBm	20 dB below the peak in-band emission in any 100-kHz bandwidth	
Other	50mV/m	-1.23dBm	50μV/m	-31.23dBm

These limits come from FCC sections 15.247 and 15.249. Digitally spread refers to when the signal is spread over a spectrum using digital modulation at a high data rate or direct sequence spread spectrum techniques. An important distinction about the 2.4GHz ISM band is that an averaging detector can be used for higher output power limits. The peak spontaneous output power is allowed to be 20dB higher than the average power. The maximum output power must also comply with specific absorption rate (SAR) limitations of 1.6W/kg per 1g averaging [11].

1.2.1 Data Rate

The analog signal from the electrodes placed in the brain will need to be digitized in order to process the signal efficiently. The data rate for a certain amount of channels can be calculated using

$$\text{Data Rate} = N\,\frac{\text{samples/s}}{\text{channel}} \times C\,\text{channels} \times M\,\frac{\text{bits}}{\text{sample}} \tag{1.2}$$

The signals from the brain are on the order of 1Hz to a few hundred hertz. For an electrode array containing 32 electrodes, a 16-bit ADC, and a 4kHz sample rate, the maximum data rate would be 2.05Mbits per second. Now, using the Nyquist criteria for a noiseless channel

$$C = 2 \cdot BW \cdot \log M \tag{1.3}$$

where, C is the capacity, BW is the bandwidth, and M is the number of signaling values in the modulation scheme, the minimum bandwidth needed can be calculated. For the maximum bit rate of 2.05Mbits per second and a binary modulation scheme, the minimum bandwidth needed is 1.025MHz (or half the bit rate).

1.3 Specifications and Scope

This work is a collaboration between the University of North Carolina at Charlotte and Yale University, the goal of which is to develop an implantable system that can monitor brain activity in a rat. This system will be implanted over an extended period of time and record EEG data. Data will be sent through wireless telemetry to a base station for analysis. Contributions from this work are specifically the antenna for the implant and the base station. Anything not pertaining to the antenna or the WBAN, containing the implant and base station, are out of the scope of this thesis.

With the standards and regulations already defined a set of specifications for completion can be derived. Table 1.2 includes a summary of the specifications required for the project to be considered complete. The subject will be contained in an enclosure that is 30.48cm squared with a height of 22.86cm. The implant should fit within 2cm squared with a height of 8cm. The volume the implant should fit in is defined by an enclosure that will be constructed from alumina. The relative permittivity (ε_r) of alumina is approximately 10, which will play an important role in the design of the implant. Alumina is also chosen for its high bio-compatibility.

Table 1.2: The list of measurable specifications for successful completion

Reference	**Category**	**Min**	**Max**	**Units**	**Description**
S01	Purpose	–	–	True/False	Should be implantable in the skull of a rat
S02	Size	0x0x0	2x2x8	cm^3	Allowable implant dimensions
S03	Bio-Compatibility	0	1.6	W/kg	Should not exceed the FCC limit for SAR
S04	Frequency	–	–	True/False	Should deliver data in an ISM frequency band
S05	Operating Life	9	–	Months	Should operate over the time period without failure

Since the design in this work is intended for use in an EEG system the antenna will need to interface with electrodes placed in the brain. An array of electrodes was designed in [12] and will be used at the reference for the electrodes.

CHAPTER 2: BACKGROUND

2.1 Epilepsy and Neural Recording

In order to design a system that will aid in the detection of a disease it is important to have an understanding of it. In 2014 the International League Against Epilepsy (ILAE) reclassified epilepsy from a disorder to a disease and redefined it as:

1. At least two unprovoked (or reflex) seizures occurring >24 h apart
2. One unprovoked (or reflex) seizure and a probability of further seizures similar to the general recurrence risk (at least 60%) after two unprovoked seizures, occurring over the next 10 years
3. Diagnosis of an epilepsy syndrome

Being reclassified as a disease emphasizes epilepsy as a lasting ailment[13]. Seizure activity can be monitored with a continuous electroencephalogram (cEEG) test, where electrodes are placed on the scalp, and it has been shown to detect seizures in 19% of patients [14]. Sample data from a cEEG can be seen in figure 2.1.

Similar to an EEG, data from an iEEG (intercranial EEG) is collected through electrodes placed within the brain. Epilepsy is characterized by abnormal firing of neurons and the electrodes can capture the signals produced. The monitoring and capture of the iEEG data is extremely useful because seizures can be detected electrically before they are detected clinically [16]. As shown in figure 2.2 the seizure is

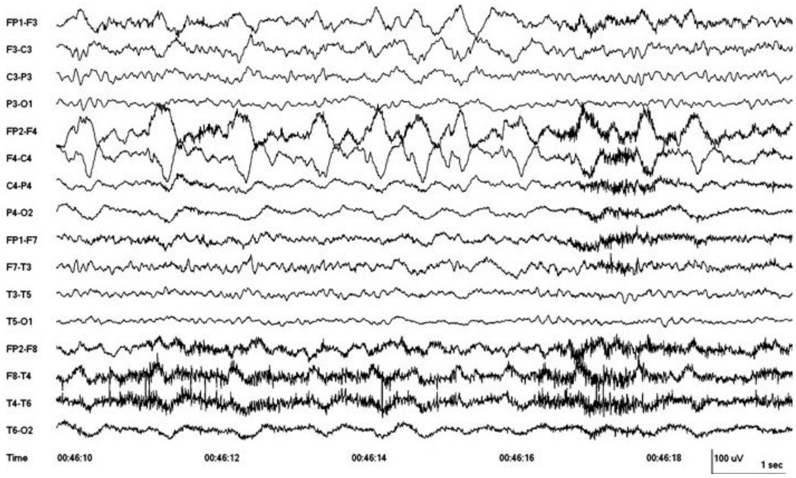

Figure 2.1: Sample EEG data from a 71-year-old man with seizures [15].

detected electrically 7.5 seconds before it is detected clinically.

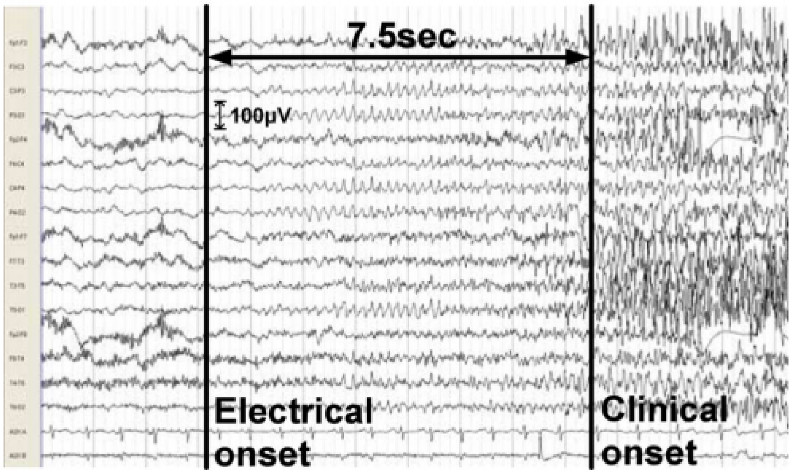

Figure 2.2: Sample EEG data that shows the difference in electrical and clinical onset [16].

2.2 The Near and Far Field

To begin the discussion of radiators and their use as antennas, the effects of the fields at all distances is investigated. For the purposes of this example an electric dipole source is used. For a dipole radiator to be an antenna, there must be a current produced and that current must be time dependant. An electric dipole is defined as two equal and opposite charges, Q_0, with some sinusoidal time dependence, separated by a distance Δl. The electric dipole moment is defined as $p = Q_0 \Delta l e^{j\omega t} \hat{z}$ when the current, I, between the charges is traveling in the z direction. The magnetic vector potential of an infinitesimal segment of current, some distance r away, is integrated and the potential is given by

$$A = \frac{\mu_0 I \Delta l'}{4\pi r} \hat{z} \tag{2.1}$$

The wave equation,

$$-\nabla^2 A = \mu J - \mu\epsilon \frac{\partial^2 A}{\partial t^2}, \tag{2.2}$$

is now solved producing the spherical components of the electric and magnetic field as:

$$E_r = 2Pe^{-j\beta r} cos\theta \left(\frac{1}{(j\beta r)^2} + \frac{1}{(j\beta r)^3} \right) \tag{2.3}$$

$$E_\theta = Pe^{-j\beta r} sin\theta \left(\frac{1}{j\beta r} + \frac{1}{(j\beta r)^2} + \frac{1}{(j\beta r)^3} \right) \tag{2.4}$$

$$H_\phi = Pe^{-j\beta r} sin\theta \left(\frac{1}{j\beta r} + \frac{1}{(j\beta r)^2} \right) \tag{2.5}$$

where,

$$P = -\frac{\eta I_0 \beta^2 \Delta l'}{4\pi} \tag{2.6}$$

Here, r is the radial distance away from the source, β is the wavenumber defined as $\beta = 2\pi/\lambda$, and η is the wave impedance $\eta = \beta/\omega\varepsilon$. These are the equations that describe the electric and magnetic field at all distances in space away from the electric dipole. The $1/r$ dependence in these equations show that there is three distinct regions of space: the near field (r^3), the "transition zone" (r^2), and the far field (r). The "transition zone" plays no real role in the investigation and will be ignored [17].

2.2.1 Considering The Near Field

The near field is defined as the region of space with the inverse cubic dependence on the radial distance. Because the wavenumber, k, is constant the first r term in equations (2.3,2.4,2.5) becomes dominant. When $k = 2\pi/\lambda$ then the following condition must be satisfied

$$\frac{1}{kr} \ll \frac{1}{(kr)^2} \ll \frac{1}{(kr)^3} \tag{2.7}$$

or in other words

$$r \ll \frac{\lambda}{2\pi} \tag{2.8}$$

Essentially, the near field is that location that is much smaller than a wavelength away. This dependence simplifies the expressions for the fields as

$$H_\phi = \frac{I_0 \Delta l'}{4\pi r^2} sin\theta \tag{2.9}$$

$$E_\theta = \frac{Q\Delta l'}{4\pi\varepsilon r^3} sin\theta \tag{2.10}$$

$$E_r = \frac{Q\Delta l'}{2\pi\varepsilon r^3} cos\theta \tag{2.11}$$

This produces fields that are identical to an electrostatic dipole, if the dipole moment is substituted in ($p = Q\Delta l$), except that the charge is a phasor. This shows that propagation does not occur in the near field and the effect is energy storage. The stored electric field energy is much higher than the stored magnetic field energy in the near field [17] and this effect becomes prevalent in section 3.3.1.

2.3 Specific Absorption Rate

When tissues are placed in the proximity of EM radiation a useful metric is SAR (specific absorption rate). Since all tissue is conductive at some level then some of the radiated EM energy will be absorbed by the tissue. If the tissue absorbs too much energy it can damage the biological system. Thus, SAR is the maximum amount of energy that a specific mass can absorb safely. As stated previously, the maximum allowable SAR level for human tissue is 1.6W/kg per 1g averaging.

From [18] an accurate definition for SAR in tissue can be derived. The expression for SAR is typically the ratio of the time rate of EM energy imparted into the mass of a biological medium. The units of this expression are watts per kilogram, W/kg. In this section a uniform plane wave travelling in the $+z$ direction is given by,

$$\mathbf{E} = E(z)\hat{e_x} \tag{2.12}$$

where,

$$E(z) = E_0 e^{-\gamma z}. \tag{2.13}$$

Here, γ is the propagation constant. The average SAR is expressed by,

$$\overline{SAR} = \frac{\Delta P}{\rho \Delta V}. \tag{2.14}$$

In (2.14) this equates to the incremental power ΔP, absorbed by a mass Δm, contained in an incremental volume ΔV of density ρ. The time-averaged Poynting vector, which represents the instantaneous power due to electric and magnetic fields is represented by [19],

$$S(z) = \frac{1}{2}\mathrm{Re}\{\mathbf{E}(z) \times \mathbf{H}(z)^*\}. \tag{2.15}$$

The amplitudes of the electric and magnetic vectors decrease as they travel in lossy media. This results in the decrease of the amplitude of the Poynting vector, yielding

$$S(z) = \frac{|E_0|^2}{2} \cdot e^{-2\alpha z} \cdot \mathrm{Re}\left\{\frac{1}{\boldsymbol{\eta}^*}\right\}. \tag{2.16}$$

Here, η is the wave impedance. The incremental volume is the incremental change in the direction of propagation times the area $\Delta V = \Delta z \Delta A$ and is equal to the loss in power $-\Delta S$ for the given area. The term $\Delta z = z_1 - z_0$ and is the thickness of the medium. Therefore, the expression for incremental power can be rewritten as,

$$\Delta P = -\Delta S \Delta A. \tag{2.17}$$

Now, using 2.14,

$$\begin{aligned} \overline{SAR} &= \frac{-\Delta S}{\rho \Delta z}, \\ &= \frac{|E_0|^2}{2\rho z} \cdot \left[e^{-2\alpha z_0} - e^{-2\alpha z_1}\right] \cdot \mathrm{Re}\left\{\frac{1}{\boldsymbol{\eta}^*}\right\} \end{aligned} \tag{2.18}$$

Using the derivative of 2.16 the general expression for SAR is

$$SAR(z) = \frac{\alpha |E(z)|^2}{\rho} \cdot \mathrm{Re}\left\{\frac{1}{\boldsymbol{\eta}^*}\right\}. \tag{2.19}$$

Where, α is the real part of γ and is defined as the attenuation constant and given by

$$\alpha = \omega\sqrt{\mu\varepsilon}\sqrt{\frac{1}{2}\sqrt{s + \left(\frac{\sigma}{\omega\varepsilon}\right)^2} - \frac{1}{2}}. \tag{2.20}$$

This is a useful general equation for SAR, but it lacks practicality. A simplified equation for peak SAR is presented in [20] as

$$SAR = \frac{\sigma E^2}{2\rho} \tag{2.21}$$

where σ is the conductivity, E is the electric field strength, and ρ is the mass density. From this simple equation it can be seen that SAR is simply a measure of how much of the electric field is absorbed by the tissue. Because the electric field changes with radial distance, these are all functions of the distance away from the radiator. The electric field radiated from the antenna in the implant can be calculated and used to calculate the SAR in surrounding tissues. This leads to the notion of a spatial average SAR. The definition of SAR includes mass and volume limitations and from [11] it is shown that the spatial average SAR is

$$SAR = \frac{1}{\mathrm{mass}(V)} \int_V \frac{\sigma(r)|E(r)|^2}{2} \mathrm{dv} \tag{2.22}$$

Even with these equations, [21] demonstrates that the calculation of SAR, especially in brain tissue, is no trivial matter. There are multiple methodologies on calculating SAR and a detailed tissue model is needed to accurately calculate it.

In simulation, SAR is typically measured by inserting a specific anthropomorphic mannequin (SAM) model into the design and calculating the E-field present in the model. The SAM model is a conservative representation of a real human head that aims to simplify the simulation of biological tissue. Because this thesis aims to implant an antenna in a rat's head, instead of a human's head, there is not a SAM model readily available. Therefore, tissues need to be created in the simulation software to model those found in the head of a rat. The IEEE SAM model and its degree of simplification is discussed in [22] where it is found that it is not always adequate. Designing the tissues with specific cases in mind should prove to be a better representation of real world effects.

The length of the antenna also affects the SAR, as shown in [23], where a longer antenna resulted in a lower SAR. The physically longer antenna resulted in a more even distribution of the electric field across the radiator and thus a lower SAR. The ground plane size also affects the SAR in that a larger ground plane can influence the measured SAR significantly. Shown in [24], a larger ground plane ($L > 0.8\lambda$) results in a lower SAR in the 1g and 10g models. The ground plane effect also shows that when the radiator is closer to the tissue than the ground plane that the SAR is increased, especially when the ground plane is larger.

2.4 Antenna Radiation Pattern

An important parameter to antenna performance is the radiation pattern. The radiation pattern is defined as a mathematical function or graphical representation in terms of space coordinates. This is usually done in the far field and can be represented by the field strength, directivity, or radiation intensity. A convenient coordinate system to view the radiation pattern is the polar system which is shown in figure 2.3.

The radiation pattern of an antenna will be made of lobes, which represent the regions of the radiation pattern bounded by very low values. The major lobe is usually the one of interest and from the major lobe two definitions can be made: half-power beamwidth (HPBW) and first null beamwidth (FNBW). Figure 2.4 shows a graphical representation of the two, where HPBW is defined as 3dB down from the

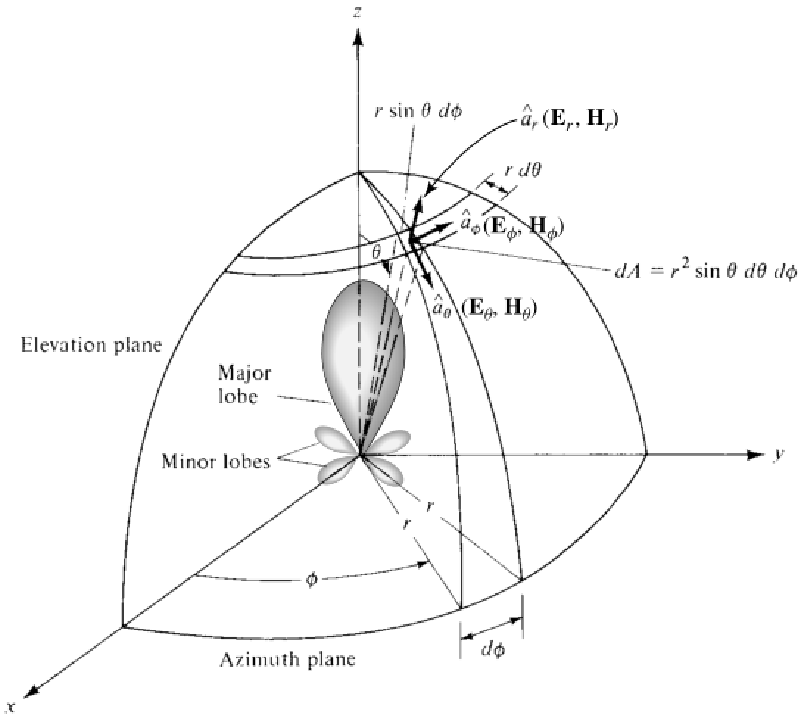

Figure 2.3: Polar coordinate system for antenna analysis [25].

peak and FNBW is defined as the distance between the first nulls (zeros).

2.5 Directivity

The definition of directivity is "the ratio of the radiation intensity in a given direction from the antenna to the radiation intensity averaged over all directions. The average radiation intensity is equal to the power radiated by the antenna divided by 4π. If the direction is not specified, the direction of maximum radiation intensity is implied."[25]. This is relative to an isotropic radiator, which is a theoretical radiator that radiates the same intensity in all directions. Mathematically, the radiation intensity of an isotropic radiator is

$$U_0 = \frac{P_{rad}}{4\pi}. \tag{2.23}$$

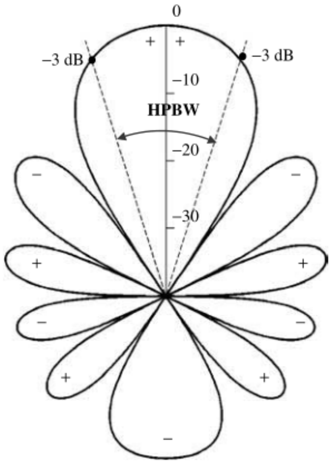

Figure 2.4: Radiation pattern of power (in dB) [25].

Here, 4π is the solid unit angle of an entire Euclidean sphere, $U(\theta, \phi)$ is the radiation intensity (W/unit solid angle), P_{rad} total radiated power (W), which makes directivity unitless. Therefore, the intensity is simply the radiated power over 4π steradians (which is the solid angle for a full sphere). By definition directivity is the ratio of radiation intensity of a given antenna to that of an isotropic radiator, given by

$$D(\theta, \phi) = \frac{U(\theta, \phi)}{U_0} = \frac{4\pi U(\theta, \phi)}{P_{rad}}. \tag{2.24}$$

The function of radiation intensity, $U(\theta, \phi)$, is the radiated power per unit angle. From [26], this does not include losses or reflections and is related to the far field by

$$U(\theta, \phi) = \frac{1}{2\eta}[|E_\theta(\theta, \phi)|^2 + |E_\phi(\theta, \phi)|^2]. \tag{2.25}$$

Integrating (2.25) the radiated power in a given direction is found by,

$$U(\theta) = \int_0^{2\pi} U(\theta, \phi) d\phi. \tag{2.26}$$

For this integral the function $U(\theta, \phi)$ must be known for the entire sphere.

2.6 Gain

Since directivity does not take the efficiency of the antenna into account, the metric of gain is also used. From [25] the total efficiency of an antenna is

$$e_0 = e_r e_c e_d \tag{2.27}$$

where

e_0 = total efficiency

e_r = reflection efficiency = $(1 - |\Gamma|^2)$

e_c = conduction efficiency

e_d = dielectric efficiency

Γ = voltage reflection coefficient at the input terminal

2.7 Electrically Small Antennas

Because the purpose of the antenna designed in this work is to be implanted into a host, the need for miniaturization is paramount. Miniaturized antennas, or electrically small antennas (ESA), are characterized by unique challenges. An in depth look at the challenges behind designing an ESA is done in [27] where it is shown that gain, bandwidth, efficiency, and polarization purity are all affected by miniaturization.

High dielectric materials are often used to miniaturize an antenna. The high relative permittivity of these materials leads to less energy being radiated away and more energy being trapped under the radiator in the dielectric. This can severely impact the efficiency of an ESA.

The well known Wheeler-Chu limit [28] was further extended by Harrington [29] to include losses. Because ESA feature a high amount of surface current, over more electrically standard antennas, the resistive loses will be higher.

PIFA antennas are particularly susceptible to low polarization purity because the current going into the shorting section will be perpendicular to the current of the radiating edge. This leads to cross polarization and can affect the polarization purity.

Because biological tissues are so lossy and the near field couples strongly to them, as shown in section 2.2.1, the sphere that encloses the antenna becomes ambiguous. It has been shown in [4] that nearby body parts and tissues strongly affect the performance of an implanted ESA and it then becomes hard to define what exactly the antenna is. The body parts themselves could be considered part of the antenna and would modify the parameters for expressions to calculate the challenges of an ESA as defined by Wheeler, Chu, Harrington and others [30].

CHAPTER 3: ANTENNAS IN LOSSY MATTER AND BIOLOGICAL TISSUE

3.1 Dielectrics and Polarization

The interaction of materials and electromagnetic energy is typically divided into two groups: conductors and dielectrics. Dielectric materials are those where the charges contained in the material are not free to move. Although the charge is not free to move, the molecules themselves can move, therefore some movement exists. For this discussion dielectrics will be "perfect", meaning that they have no free charges, but they are all bound.

3.1.1 Polarization

Molecules in a dielectric may be viewed as positive and negative charges in a charge neutral configuration. According to Gauss' law, the external electric field of each of these molecules is zero; although, the negative electrons and positive nucleus produce internal fields. If an external electric field is then applied to the dielectric then the field will apply a force on the positive and negative charges, polarizing the material. The polarization of the charges results in an electric dipole that, according to Coulomb's law, aligns itself with the external field. Each molecule inside the dielectric now produces a dipole moment and the total moment of the material depends on the number of moments and the strength of each one. A dipole moment is defined as the vector that points from the negative charge to the positive charge, which have equal and opposite charges. Therefore, the dipole moment is a measure of the overall polarity of the system and has units of Coulomb-meter (C·m). The internal dipole moments in the dielectric sum together to create an internal field that is in the opposite direction of the external field, meaning the internal field has a much lower magnitude. However, not all of the dipole moments align in the same way in a real material. The opposition of the internal and external fields results in a results in a reduced electric field intensity inside the material.

The polarization vector is described by

$$\mathbf{P} = \lim_{\Delta v \to 0} \frac{1}{\Delta V} \sum_{i=1}^{N} \mathbf{p}_i \quad \left[\frac{\mathrm{C}}{\mathrm{m}^2}\right] \tag{3.1}$$

While this is a useful expression and puts the previous discussion into context, it is generally not able to be calculated because it depends on the polarization of individual molecules. Also, because molecules closer to the surface are more strongly affected by the external field not all the molecules will have the same polarization. This leads to the notion that there is surface and volume charge densities present in the material. These values are also not readily calculable, but if they are assumed to be known then the electric field anywhere in space. It can be shown that the polarization vector relates to the electric field by

$$\mathbf{D} = \varepsilon_0 \mathbf{E} + \mathbf{P} \tag{3.2}$$

Because the polarization adds to the electric displacement field in the absence of polarization it is best to view it as a means to decrease the electric field intensity in the dielectric. Polarization depends on an external electric field and therefore can be re-written as

$$\mathbf{P} = \varepsilon_0 \chi_e \mathbf{E} \tag{3.3}$$

The parameter, χ_e, is electric susceptibility and is a measure of how susceptible a material is to being polarized. If (3.3) is substituted into (3.2) it is written as

$$\mathbf{D} = (\varepsilon_0 + \varepsilon_0 \chi_e)\mathbf{E} \tag{3.4}$$

The factor multiplied with the electric field is now re-written as

$$\varepsilon = (\varepsilon_0 + \varepsilon_0 \chi_e) = \varepsilon_0(1 + \chi_e) = \varepsilon_0 \varepsilon_r \tag{3.5}$$

Which, results in the familiar constitutive relation

$$\mathbf{D} = \varepsilon_0 \varepsilon_r \mathbf{E} = \varepsilon \mathbf{E} \tag{3.6}$$

Here, ε_r is the relative permittivity. This is a much more useful term than susceptibility because the susceptibility is not easy to measure and the relative permittivity can be directly measured. Now a simple relationship between the displacement field and the electric field exists with the relative permittivity of a material being the proportion.

3.1.2 Material Parameters

Materials not only have an electric response, but a magnetic one known as permeability μ. The permittivity ε, permeability μ, and conductivity σ of a linear, homogeneous, isotropic material are complex quantities given by

$$\varepsilon = \varepsilon_0(\varepsilon'_r - j\varepsilon''_r) \tag{3.7}$$

$$\mu = \mu_0(\mu'_r - j\mu''_r) \tag{3.8}$$

$$\sigma = \sigma' - j\sigma'' \tag{3.9}$$

Body tissue does not have a magnetic response and the relative permeability is $\mu_r = 1$ and $\mu'' = 0$. Because there is no magnetic response, the real part of the two equations (3.7) and (3.9) are

$$\varepsilon'_e = \varepsilon'_r - \frac{\sigma''}{\omega\varepsilon_0} \tag{3.10}$$

$$\sigma'_e = \sigma' + \omega\varepsilon_0\varepsilon''_r \tag{3.11}$$

Using Maxwell's equations the complex permittivity ε_e is defined as

$$\varepsilon_e = \varepsilon_0(\varepsilon'_e - j\varepsilon''_e) = \varepsilon_0\left(\varepsilon'_e - j\frac{\sigma'_e}{\omega\varepsilon_0}\right) \tag{3.12}$$

The power dissipated in the medium is described by the loss tangent referred to as tanδ, where δ is the skin depth, shown by

$$\tan\delta = \frac{\varepsilon''}{\varepsilon'} \tag{3.13}$$

Now, using the constitutive equations shown in this section, expressions for the wave number k_e and the wavelength λ_e inside the dielectric are

$$k_e = \omega\sqrt{\mu_0\varepsilon_0}\sqrt{\varepsilon'_e - j\frac{\sigma'_e}{\omega\varepsilon_0}} \quad \lambda_e = \frac{2\pi}{\omega\sqrt{\mu_0\varepsilon_0}}\mathrm{Re}\left\{\sqrt{\frac{\omega\varepsilon_0}{\omega\varepsilon_0\varepsilon'_e - j\sigma'_e}}\right\} \tag{3.14}$$

Because some of these constants require an understanding at the atomic level it is useful to consider ε_r'' and σ'' to be zero. As well as using the common notation that $\sigma_e' = \sigma'$. In this thesis the work of Gabriel in [31] is used for characterization of tissue and these equations and considerations align with his work.

3.2 Modeling Equations for Tissue

As was described in previous sections, materials are electrically defined by their permittivity ε and their permeability μ. To describe the behavior of the permittivity in certain materials the Cole-Cole equation can be used. The Cole-Cole equation is a more specific case of the Debye equation. These are relaxation equations that describe the time change in permittivity due to changes in frequency and field strength. The purpose of this work is to develop a system that will be implanted into live tissue and therefore the dielectric properties of the tissues of a rat need to be taken into consideration. The features of tissues have been reviewed and characterized in [32] and further parameterized in [31]. The work done by Gabriel in [31] uses the four parameter Cole-Cole equation, which is considered the most precise way to describe the relaxation of a dielectric.

Polarization and dielectric relaxation were first described by Debye in [33]. In this Debye explains the electric dipole moment and the torque applied on it by the external electric field. A brief summary of polarization is found in section 3.1.1. Here, the mechanisms for bulk polarization of a material are described and parameterized. An important parameter is the relaxation time τ, which is the time it takes for the dipole moments in the material to revert back to a random state after the external field is removed. The work done by Gabriel characterizes tissue from 10Hz-100GHz and over that frequency range are relaxation regions. These regions represent different polarization mechanisms that are all functions of the time constant τ. Debye represents the polarization mechanism in the material by viscous damping and leads to the expression

$$\hat{\varepsilon} = \varepsilon_\infty + \frac{\varepsilon_s - \varepsilon_\infty}{1 + j\omega\tau} \tag{3.15}$$

In this Debye expression the term ε_∞ is the permittivity at very high frequencies and the term ε_s is the permittivity at very low frequencies. The magnitude of the dispersion is expressed as $\Delta\varepsilon = \varepsilon_s - \varepsilon_\infty$. A more specific case of the Debye model, which accounts for dispersion of lossy materials, is the Cole-Cole model given by,

$$\hat{\varepsilon} = \varepsilon_\infty + \frac{\varepsilon_s - \varepsilon_\infty}{1 + (j\omega\tau)^{1-\alpha}} + \frac{\sigma}{j\omega\varepsilon_0} \tag{3.16}$$

In these expressions for permittivity the term ε_∞ is the permittivity at frequencies where $\omega\tau \gg 1$, ε_s is the permittivity at $\omega\tau \ll 1$, $j^2 = -1$, σ is a conductivity term, and ε_0 is the permittivity of free space. The complex permittivity is expressed as $\hat{\varepsilon} = \varepsilon' - j\varepsilon''$, where ε' is the relative permittivity and $\varepsilon'' = \sigma/\omega\varepsilon_0$. This means that the real part of the complex permittivity is the relative permittivity and the imaginary part can be used to calculate the conductivity.

There are three main relaxation regions α, β, and γ for low, medium, and high frequencies respectively, as well as δ for minor dispersions. A relaxation in a dielectric refers to the time delay between a change in the electric field and a change in the polarization. This is analogous to hysteresis in magnetic materials. The low frequency α region is representative of the ionic diffusion in cell membranes. Over the hundreds of kilohertz range, the β dispersion is due to the polarization of the cell membranes. Finally, in the high frequency gigahertz range, the γ dispersion is due to the polarization of water molecules found in the tissue [34].

Hurt shows in [35] that beyond 5 relaxation regions, for a Debye model, there is little to be gained. For this reason, Gabriel suggests in [31] that the Cole-Cole model will accurately describe biological tissue, with addition of the α term (not to be confused with the relaxation region), which represents a broadening of the dispersion spectra. These relaxations are functions of the electric field's frequency ω. The main focus for this work is the γ relaxation as it extends into the GHz range.

3.2.1 Cole-Cole Parameters for Rat Tissue

From [34] it is shown that the water content of a rat's tissue changes with age. The water content directly effects the γ relaxation and therefore the permittivity of the tissue. Table 3.1 summarizes the Cole-Cole parameters for the tissues in rats as they age. The ± terms correspond to a 95% confidence interval from the experimental testing.

These functions of permittivity bring about a challenge in the design of an implant in that the intrinsic impedance is a function of the relative permittivity. The parameters given in the table are used in the Cole-Cole equation, fixed at 2.45GHz, and the relative permittivity and conductivity for the different tissues are plotted against age in figure 3.1.

This shows that over the first 70 days of a rat's life the water content, and therefore

Table 3.1: Summary of Cole-Cole parameters for rat tissues with respect to age. Taken at 37°C and with a 95% confidence interval [34]

Tissue/age	ε_s	$\pm\varepsilon_s$	τ_{relax} (ps)	$\pm\tau_{relax}$ (ps)	α	$\pm\alpha$	σ (S m^{-1})	$\pm\sigma$ (S m^{-1})
Brain								
New born	65.0	0.3	8.23	0.30	0.11	0.01	0.140	0.002
10 days	60.0	0.3	8.06	0.29	0.10	0.01	0.130	0.002
20 days	49.4	0.4	7.83	0.46	0.18	0.02	0.110	0.003
30 days	49.7	0.4	8.31	0.47	0.18	0.02	0.098	0.003
50 days	45.8	0.5	8.38	0.56	0.19	0.02	0.091	0.003
70 days	44.8	0.3	9.40	0.38	0.12	0.01	0.086	0.002
Skull								
New born	39.9	0.2	9.21	0.31	0.17	0.01	0.097	0.001
10 days	32.5	0.3	10.05	0.43	0.24	0.01	0.06	0.001
20 days	30.2	0.5	11.04	1.03	0.25	0.03	0.05	0.003
30 days	27.1	0.6	12.72	1.49	0.28	0.03	0.042	0.003
50 days	27.8	1.0	13.55	2.96	0.32	0.04	0.036	0.005
70 days	18.3	0.3	15.60	1.44	0.22	0.02	0.024	0.001
Skin								
New born	58.68	0.23	8.22	0.22	0.15	0.009	0.143	0.002
10 days	40.48	0.17	8.81	0.24	0.12	0.01	0.099	0.001
20 days	36.58	0.46	9.32	0.71	0.21	0.03	0.086	0.003
30 days	36.35	0.59	9.44	0.89	0.24	0.03	0.079	0.003
50 days	31.12	0.30	11.08	0.60	0.15	0.02	0.069	0.002
70 days	31.06	0.19	12.27	0.42	0.11	0.01	0.066	0.001
Muscle								
New born	68.81	0.24	8.41	0.20	0.10	0.009	0.182	0.002
10 days	62.63	0.33	9.00	0.31	0.10	0.01	0.154	0.003
20 days	50.70	0.27	8.64	0.28	0.18	0.01	0.136	0.002
30 days	52.33	0.39	10.00	0.41	0.21	0.01	0.119	0.002
50 days	50.24	0.35	10.51	0.42	0.14	0.01	0.12	0.002
70 days	49.64	0.33	12.21	0.41	0.10	0.01	0.109	0.002

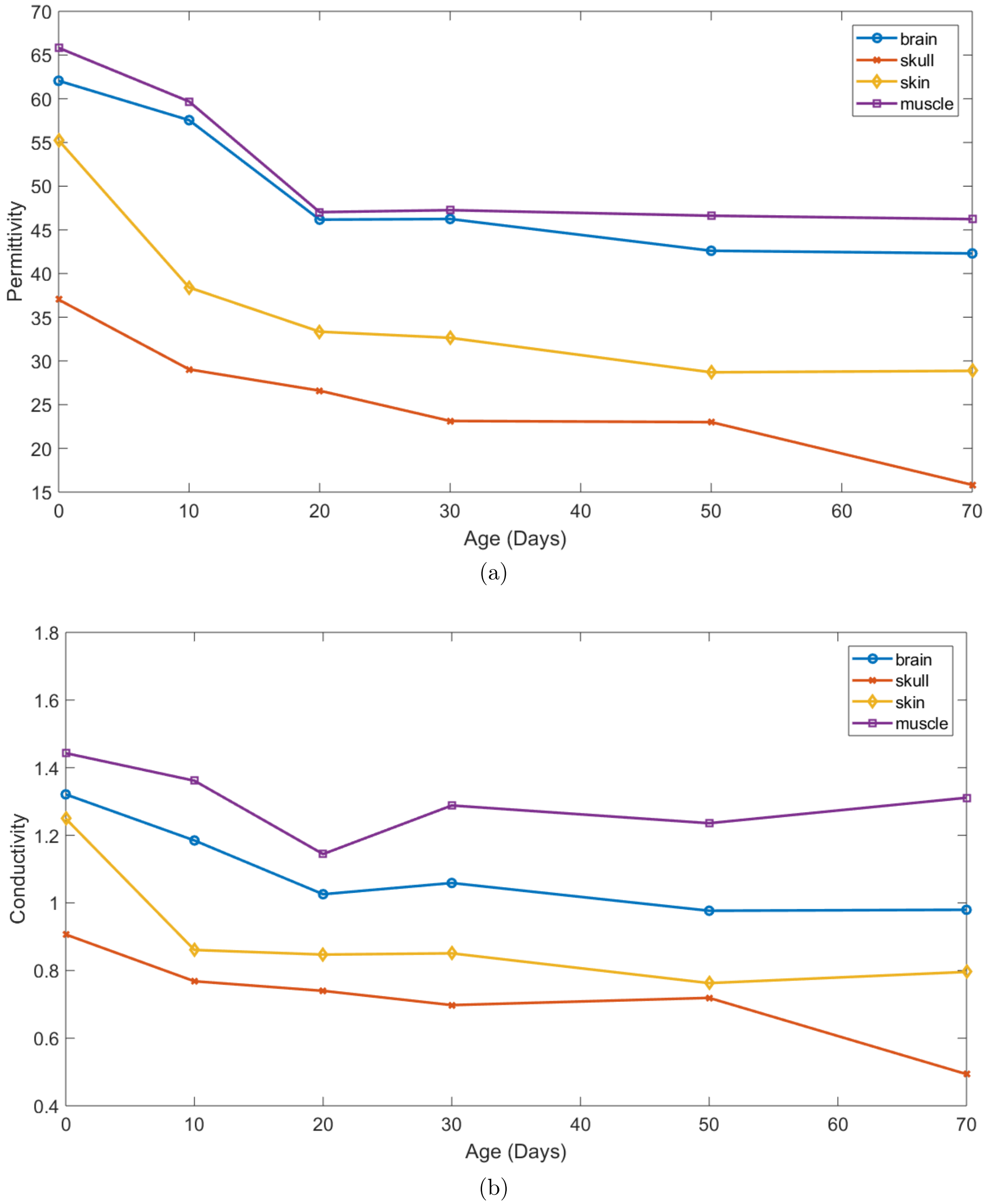

Figure 3.1: (a) Permittivity and (b) conductivity for different rat tissues versus age at 2.45GHz

the permittivity, changes by around 30-50%. If the permittivity of the rat's tissues are changing with age then the best practice would be to use a rat that is older than

70 days. Using the Cole-Cole equation and the values provided in table 3.1 the plots of relative permittivity and conductivity for relevant tissue over frequency are given in figure 3.2.

Plotting the permittivity over frequency shows that is is constant over the entire ISM band. This means that to simulate the phantoms that the Cole-Cole model does not need to be entered, but simply a number. The conductivity does not appear to be flat over frequency and the change across frequency for the different tissues is shown in table 3.2.

Table 3.2: Conductivity at the low and high frequencies of the ISM band and the percent difference across the band for rat tissues.

Tissue	**$\boldsymbol{\sigma}$ @2GHz$\left(\frac{S}{\mathrm{m}}\right)$**	$\boldsymbol{\sigma}$ @3GHz$\left(\frac{S}{\mathrm{m}}\right)$	% **Difference**
Brain	1.317	1.344	2.03
Skull	0.523	0.541	3.38
Skin	1.029	1.051	2.12
Muscle	1.686	1.722	2.11

3.3 Antennas in Lossy Matter

Because the design in this work is intended to implanted into a biological subject, the effects of the body on the antenna are one of the main aspects of design. This section aims to to discuss the modification of antenna properties when embedded in biological tissue. Using the model discussed in section 3.2 and the resulting dielectric properties a tissue "phantom" can be constructed in simulation software to investigate the effects on an antenna.

Biological tissue, and its corresponding dielectric response, have a strong effect on a radiating element. The, typically, high relative dielectric constant of a tissue results

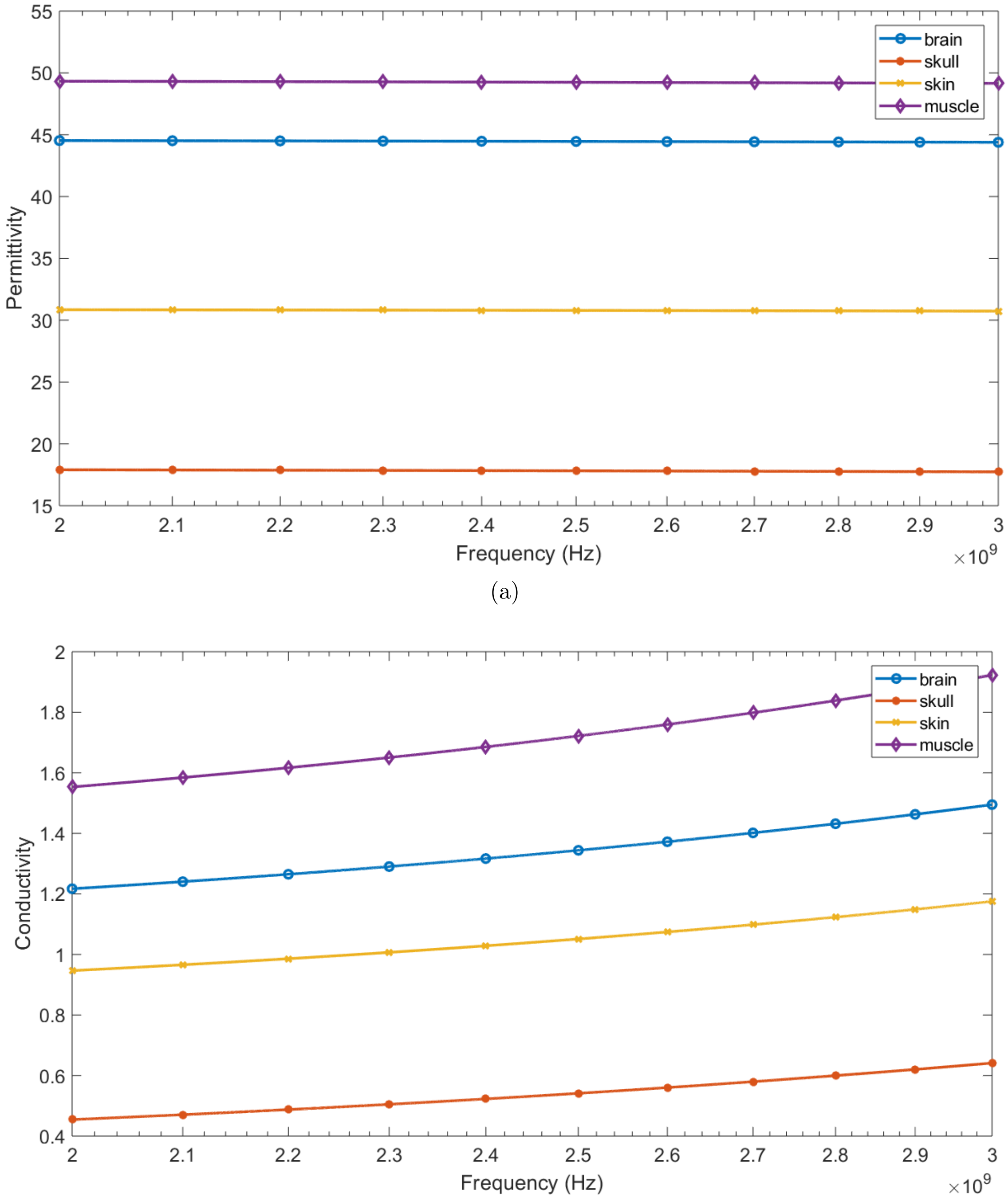

(a)

(b)

Figure 3.2: (a) Permittivity and (b) conductivity for 70 day old rat using data from [34].

in a lower resonant frequency for fixed sized antennas. The antenna will need to be made larger to keep the resonant frequency constant. This effect is presented in

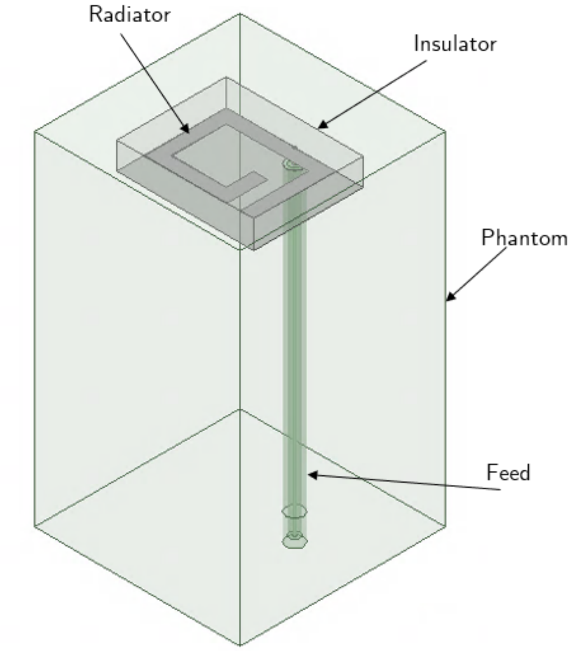

Figure 3.3: Antenna proposed in [4] shown inside insulating material and a surrounding phantom.

[4], in which a spiral microstrip antenna is constructed and placed in a fluid which resembles the dielectric properties of human skin. The antenna proposed by Kim in [4] is shown in figure 3.3. The antenna is inside of a bio-insulating material and then this is placed inside a lossless skin phantom.

Reflection coefficients, simulated in HFSS, for the antenna surrounded by free space and the phantom are shown in figure 3.4. The phantom had a relative permittivity $\varepsilon_r = 49.6$ and this shows how the dielectric loading effect of the phantom produces a downward frequency shift of the resonance. Because the phantom is lossless it presents a simple dielectric loading effect. When losses are applied to the phantom then the current in the antenna may be altered, resulting in altered radiation performance. This change in the current distribution and the radiation performance explicitly demonstrates the need for an insulation layer around the antenna. Insulat-

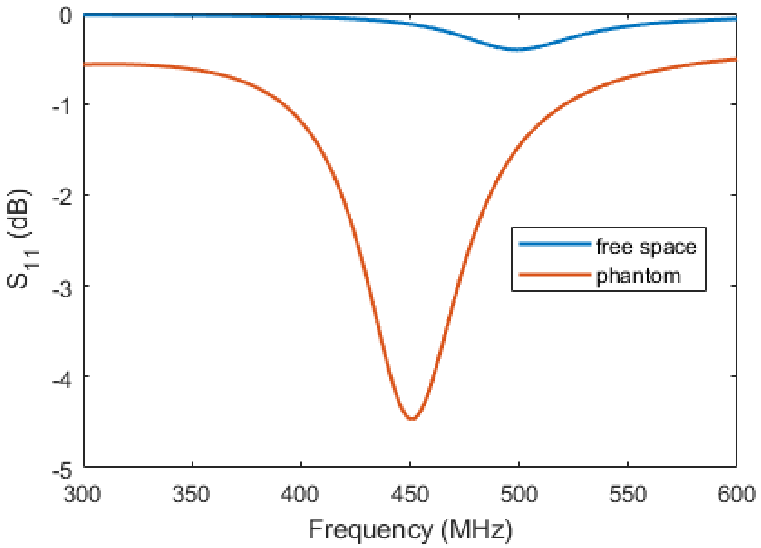

Figure 3.4: Simulated reflection coefficients of the work done in [4] where the radiator is placed in free space and a lossless tissue phantom.

ing the antenna makes it less sensitive to placement in the body.

3.3.1 Power and Efficiency in Lossy Media

One of the major effects that lossy media has on a radiator is the amount of power that it radiates. Consider the expression for the source power in a system

$$\begin{aligned} P_{source} &= P_{rad} + P_{abs} \qquad (3.17)\\ &= \oint_{S_r} \text{Re}\{\mathbf{S} \cdot \hat{r}\} dS + \frac{\omega}{2} \int_V \varepsilon_0 \varepsilon_e'' |\mathbf{E}|^2 dV, \end{aligned}$$

which is the average power P_{rad} out of a spherical surface S_r of volume V, in which there is power being absorbed, P_{abs}, and $\mathbf{S}$ is the Poynting vector. This expression can be broken up into the near field and far field expressions as

$$\begin{aligned} P_{source} &= \oint_{S_r} \text{Re}\{\mathbf{S}(1/r^2) + \mathbf{S}(1/r^n)\} \cdot \hat{r} dS + \frac{\omega}{2} \int_V \varepsilon_0 \varepsilon_e'' \big[|\mathbf{E}|^2(1/r^2) + |\mathbf{E}|^2(1/r^n)\big] dV \\ &= P_{radFF} + P_{radNF} + P_{absFF} + P_{absNF} \qquad (3.18) \end{aligned}$$

The $1/r$ dependency in this expression indicates the near and far field, where $1/r^2$ terms indicate the far field (FF) and higher order terms indicate the near field (NF) components (see section 2.2). In a typical free space scenario, the near field is mostly reactive and will not strongly affect the radiated or absorbed power. Although, in the case of small ground planes and lossy (conductive) dielectrics, the near field may well couple with the nearby material [36]. This indicates that the presence of the tissue will increase the losses of the radiator. It is because of this that an insulator becomes mandatory when trying to radiate power out of the body, as in this thesis.

3.4 Insulating Materials

The need for an insulating material surrounding the implant has been demonstrated and now material parameters are considered. Alumina is widely used to insulate electrical components because of its high dielectric strength, low thermal conductivity, and low electrical loss. According to manufacturers [37, 38] the dielectric strength of 96% alumina is upwards of 175 (volts/mil), the thermal conductivity is as low as 1.15(W/mK), and the electrical loss ($\tan\delta$) is on the order of 1E-5 [39]. The company Coltronics [38] manufactures a potting compound, Durapot 804, which is designed for small electrical parts.

The implant can be put into a mold with potting compound poured into it. The effects of the potting compound need to be accounted for in simulation and HFSS contains a material setting for alumina. In HFSS the relative permittivity of alumina is $\varepsilon = 9.4$, which is used for this design. Coltronics does not provide specific permittivity values for the potting compound, but alumina is typically close to this value especially for high percentage compounds.

CHAPTER 4: ANTENNA DESIGN BACKGROUND

In order to facilitate the creation of a brain implant that fits within the specified dimensions an antenna topology that is compact must be chosen. In this section the design and background information of planar antennas will be discussed. Microstrip antennas are a popular choice when size is an important aspect of antenna design - notably, cellular handsets typically feature PIFA antennas, which is a variation of a microstrip patch antenna. Not only is size a concern, but compatibility with microelectronics that will be present in the implant. Components packaged in SMD or IC form are usually routed with microstrip or stripline traces when placed onto a printed circuit board (PCB). Choosing a planar microstrip antenna allows for maximum compatibility with the electronics that will be part of the implant.

4.1 Embedded Microstrip

The antennas discussed in this section will all be planar structures. A planar structure on a dielectric can be fed by multiple different feed types such as coax, microstrip, and stripline. Feeding in all these cases will be done with microstrip, since this is also a planar structure.

Because there is such a need for an insulation layer in the implant, there will be a dielectric loading effect on all of the microstrip components. Not only will this apply to the antenna, but also to the microstrip lines that feed the antenna and the components. Microstrip lines will become embedded microstrip lines and this effect will change the way that the impedance of a microstrip line is calculated. A diagram of an embedded microstrip line is shown in figure 4.1.

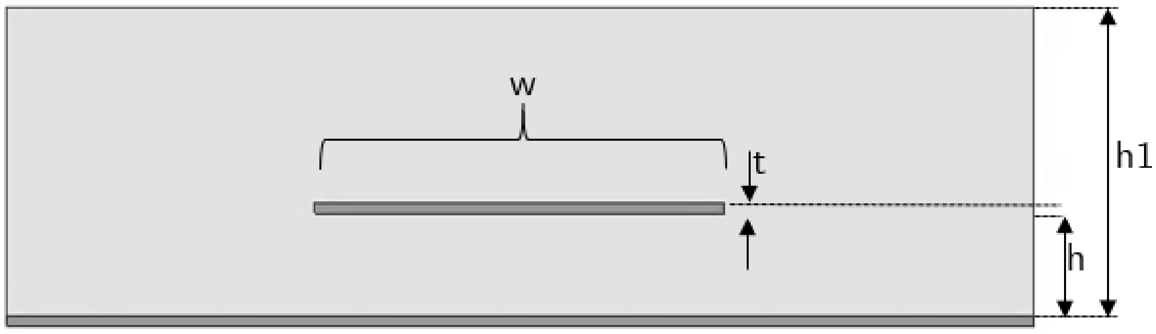

Figure 4.1: Embedded microstrip model with relevant parameters marked.

The calculation is similar to that of a normal microstrip line and is detailed below. Embedded microstrip impedance may be calculated from the following equations if the ratio of $h1/h > 1.2$

$$\varepsilon_{eff} = \varepsilon_r \cdot \left(1 - exp\left\{ - 1.55 \cdot \frac{h1}{h} \right\}\right) \tag{4.1}$$

$$Z_{0em} = \frac{60}{\sqrt{\varepsilon_{eff}}} \cdot \log\left\{5.98 \cdot \frac{h}{0.8w + t}\right\} \tag{4.2}$$

Using these equations, if the insulating layer is alumina ($\varepsilon_r = 9.4$), then the input impedance of a 0.3mm (≈ 10mil) line is 49.2Ω. This is the line width that will be used to feed the antenna.

4.2 Derivation of Microstrip Patch Antenna Model

The microstrip patch has two viable models: the transmission line and cavity models. The transmission line model offers an easier to visualize approach at the expense of accuracy. For the sake of ease, the transmission line model will be used here. A microstrip transmission line can be thought of as having two dielectrics; the actual substrate and air. Because of this the field lines do not all reside in the substrate and there are parts of field lines in the air. This can be seen in figure 4.2 and demonstrates that the line is electrically larger than it is physically. This gives rise to the effective dielectric constant ε_{reff}. The effective dielectric constant serves to be the dielectric constant of the single dielectric that would make the line electrically as big as the desired physical line. For a microstrip line that does have air as the second dielectric the value for the effective dielectric constant is in the range $1 < \varepsilon_{reff} < \varepsilon_r$. The effective dielectric constant is represented by

$$\underline{W/h > 1}$$

$$\varepsilon_{reff} = \frac{\varepsilon_r + 1}{2} + \frac{\varepsilon_r - 1}{2}\left[1 + 12\frac{h}{W}\right]^{-1/2} \tag{4.3}$$

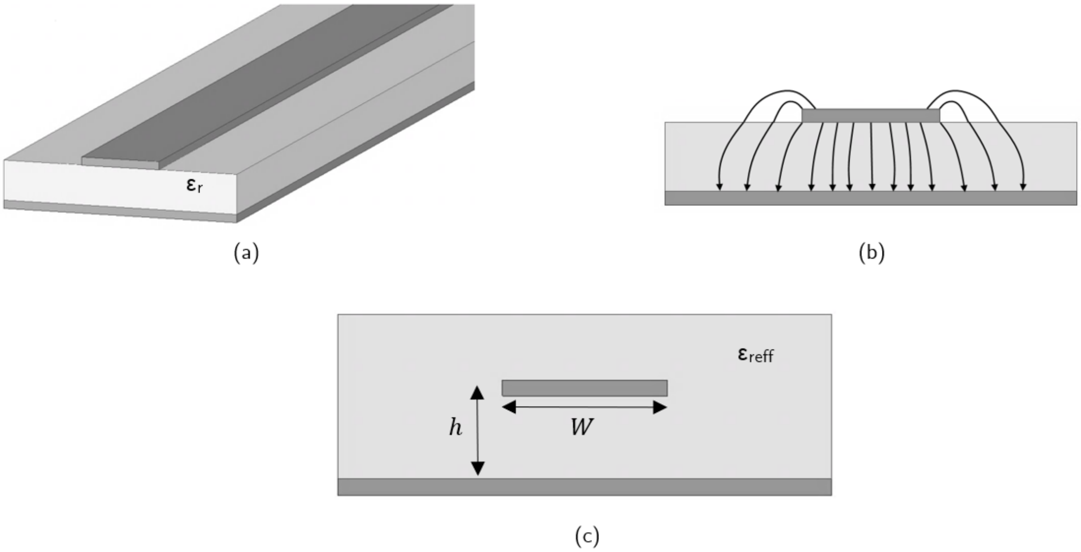

Figure 4.2: (a) A microstrip line on a substrate with relative dielectric constant ε_r. (b) Field lines associated with a microstrip line. (c) A buried microstrip line in a homogeneous dielectric represented by ε_{reff}.

This notion that a microstrip transmission line is electrically bigger than the physical line can be directly applied to a microstrip patch antenna. The physical length of a patch antenna is extended by the fringing fields at the ends of the length by Δl. This extra length is a function of the aforementioned relative dielectric constant and the ratio of the width to height (W/h). This can be seen graphically in figure 4.3 and the Δl can be solved for by

$$\frac{\Delta l}{h} = 0.412 \frac{(\varepsilon_{reff} + 0.3)\left(\frac{W}{h} + 0.264\right)}{(\varepsilon_{reff} - 0.258)\left(\frac{W}{h} + 0.8\right)}. \tag{4.4}$$

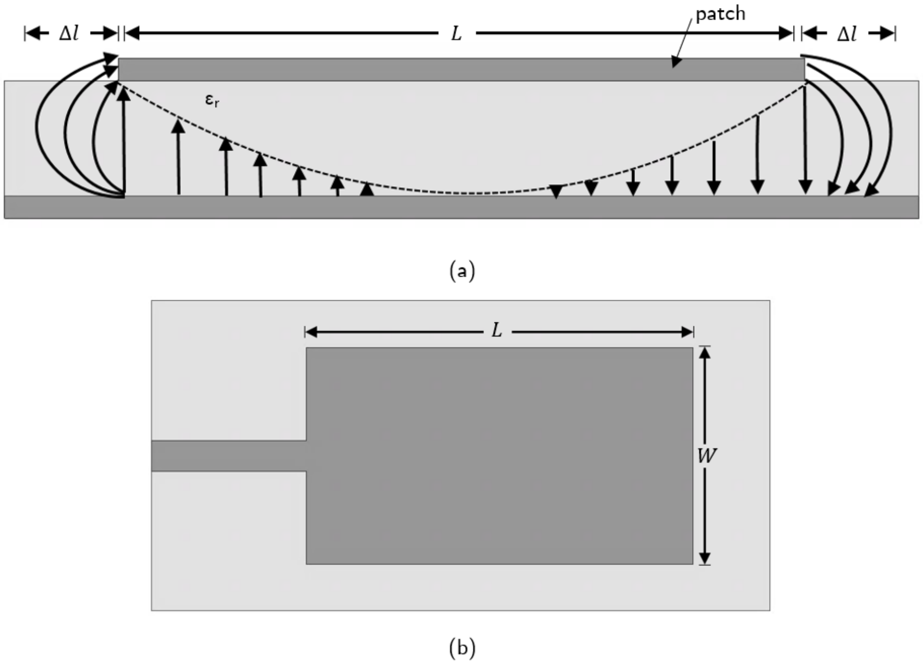

Figure 4.3: (a) Side view of a patch antenna with field lines visible. (b) Top view of a patch antenna

The extension of the length by Δl on both sides leads to an effective length of

$$L_{eff} = L + 2\Delta L \tag{4.5}$$

The resonant frequency of a patch antenna in the dominant TM_{010} mode is a function of its length and the material properties of the substrate. The usual expression for the frequency does not take the fringing effects into account and is updated by substituting L with L_{eff}. which is given by

$$(f_r)_{010} = \frac{1}{2L_{eff}\sqrt{\varepsilon_{reff}}\sqrt{\mu_0\varepsilon_0}} = \frac{1}{2(L+2\Delta L)\sqrt{\varepsilon_{reff}}\sqrt{\mu_0\varepsilon_0}} \tag{4.6}$$

These equations can be rearranged to be more useful for the design of a patch antenna. Equations (4.5) and (4.6) are rearranged to be functions of the design variables (ε_r , f_r , and h) as

$$W = \frac{1}{2f_r\sqrt{\mu_0\varepsilon_0}}\sqrt{\frac{2}{\varepsilon_r}+1} \tag{4.7}$$

$$L = \frac{1}{2f_r\sqrt{\varepsilon_{reff}}\sqrt{\mu_0\varepsilon_0}} - 2\Delta l \tag{4.8}$$

This can be used to to design a reference patch antenna. The substrate used for the antenna is Rogers TMMi 10 which has a relative dielectric constant $\varepsilon_r = 9.8$.Using equations (4.7) and (4.8) the antenna is designed to have $W = 26.33mm$ and $L = 19.55mm$. Simulating the designed antenna in HFSS results in a resonance at 2.45GHz which is shown in figure 4.4. This is too large for the specifications and needs to be miniaturized.

4.3 Miniaturization of Antennas

There are many methods to miniaturizing an antenna to make it an ESA. Spirals can provide physical length in a compact package and allow control of the reactive portion of the impedance, as in [40, 41]. The PIFA (planar inverted F antenna), adds a shorting post to a patch antenna and effectively reduces the size by half and is a popular choice for medical implants and handsets [42, 43]. Additional slots cane be

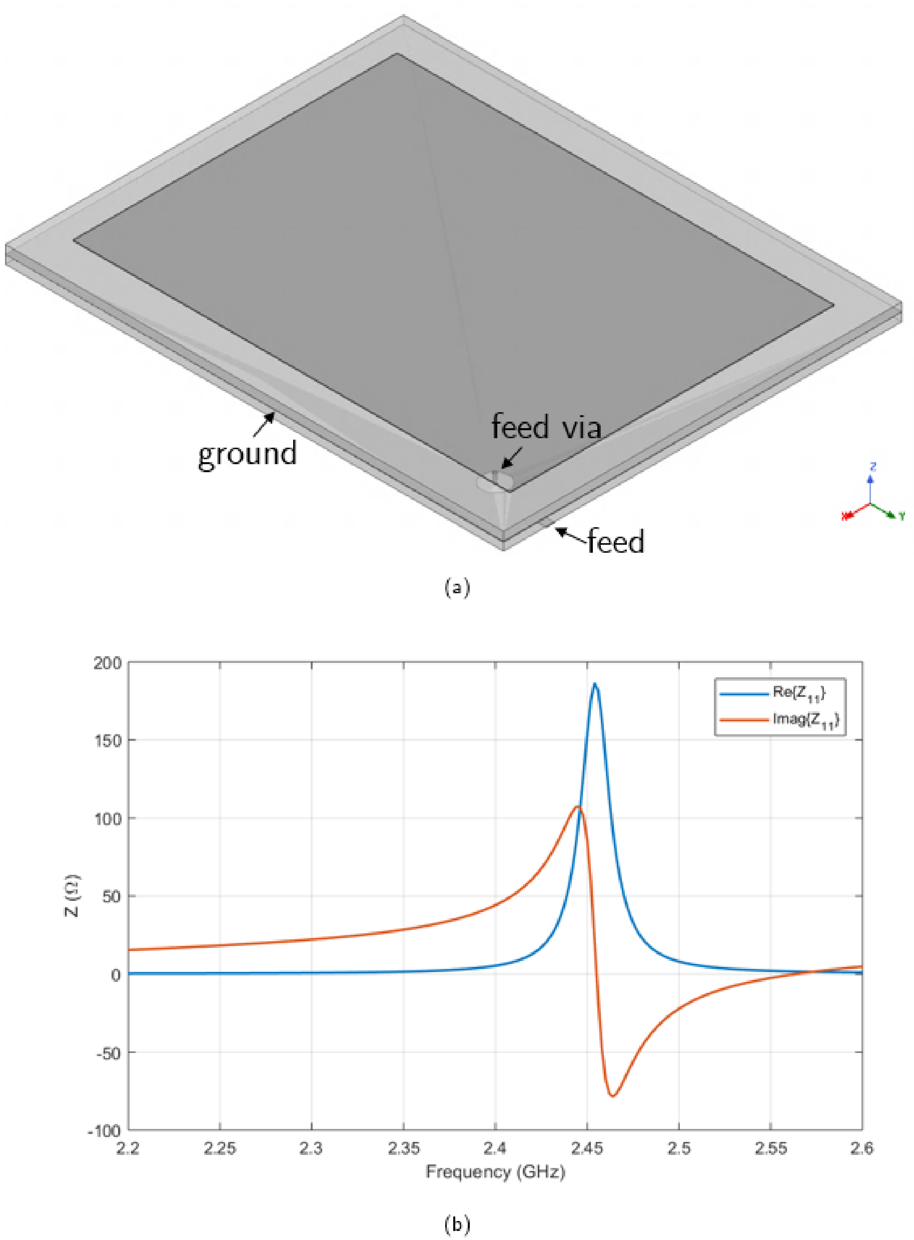

Figure 4.4: (a) HFSS model of the designed microstrip patch antenna with $W = 26.33mm$ and $L = 19.55mm$. (b) Simulated Z parameters

added to a PIFA for dual band operation or impedance control [44]. Many other techniques may be used, but the topic of interest for this thesis is the PIFA.

High permittivity materials can also be used to make an antenna electrically smaller. As shown in [45], a high permittivity material can decrease the size needed for the antenna, but can increase the losses present. Therefore, there is a sacrifice of performance for size.

4.3.1 Planar Inverted F Antennas

The transmission line model for the patch antenna is effective in designing and understanding the simple planar patch antenna. With the addition of the shorting post and the creation of a PIFA it is useful to investigate the cavity model. The patch can be modeled as a dielectric loaded cavity. When power is injected into the patch charge accumulates on the patch and on the ground plane. There are two forces that in play: an attractive and repulsive force as shown in figure 4.5.

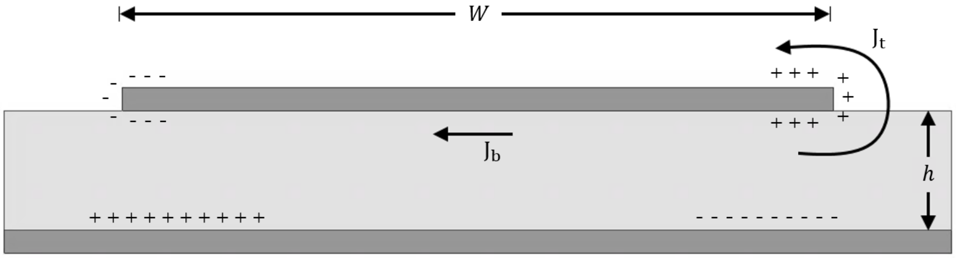

Figure 4.5: Charge distribution and currents in the patch cavity mode

The attractive force is between the charge on the bottom of the patch and the ground. This force tends to keep the charge accumulated on the bottom of the patch. The repulsive force exists between like charges on the bottom of the patch and pushes charge to the top of the patch. Since opposite charges exist on the top and bottom of the patch there is now a top and bottom current density on the patch, J_t and J_b respectively. For a typical patch the ratio h/W is very small the attractive force dominates. This makes the current density J_t very small and allows the four boundaries, defined by the edges of the patch, to be modeled as PMC surfaces (perfect magnetic conductor). The PMC boundaries ensure the normalized field modes under the patch.

Cavity mode resonance is now derived from [25]. The fields for the cavity mode must satisfy the following

$$\begin{aligned} E_x &= -\frac{1}{\varepsilon}\frac{\partial_z}{\partial y} & H_x &= -j\frac{1}{\omega\mu\varepsilon}\frac{\partial^2 F_z}{\partial x \partial z} \\ E_y &= \frac{1}{\varepsilon}\frac{\partial F_z}{\partial x} & H_y &= -j\frac{1}{\omega\mu\varepsilon}\frac{\partial^2 F_z}{\partial y \partial z} \\ E_z &= 0 & H_z &= -j\frac{1}{\omega\mu\varepsilon}\left(\frac{\partial^2}{\partial z^2} + \beta^2\right)F_z \end{aligned} \tag{4.9}$$

where F_z is a scalar potential function and is the z component of the potential function $\mathbf{F}$. This potential function must satisfy the scalar wave equation

$$\nabla^2 F_z(x, y, z) + \beta^2 F_z(x, y, z) = 0 \tag{4.10}$$

The boundary conditions on the top and the bottom of a rectangular cavity are

$$E_x(0 \leq x \leq a, y = 0, z) = E_x(0 \leq x \leq a, y = b, z) = 0 \tag{4.11}$$

$$E_z(0 \leq x \leq a, y = 0, z) = E_z(0 \leq x \leq a, y = b, z) = 0 \tag{4.12}$$

on the left and right walls they are

$$E_y(x = 0, 0 \leq y \leq b, z) = E_y(x = a, 0 \leq y \leq b, z) = 0 \tag{4.13}$$

$$E_z(x = 0, 0 \leq y \leq b, z) = E_z(x = a, 0 \leq y \leq b, z) = 0 \tag{4.14}$$

Here, the terms a and b refer to the dimensions of the cavity, where a is the width and b is the height. The potential function F_z is represented by standing waves and is written as

$$F_z(x,y,z) = A_m cos(\beta_x x) cos(\beta_y y)[C_3 cos(\beta_z z) + D_3 sin(\beta_z z)] \tag{4.15}$$

$$\begin{aligned} \beta_x &= \frac{m\pi}{a} \quad m = 0,1,2,... \\ \beta_y &= \frac{n\pi}{b} \quad n = 0,1,2,... \\ & \quad\; m \text{ and } n \text{ not both 0 simultaneously} \end{aligned} \tag{4.16}$$

Because the PIFA is a cavity resonator, there is an additional boundary condition for the front and back walls given by

$$E_x(0 \le x \le a, 0 \le y \le b, z = 0) = E_x(0 \le x \le a, 0 \le y \le b, z = c) = 0 \tag{4.17}$$

The boundary conditions are now applied and the E_x component is

$$E_x(x,y,z) = -\frac{1}{\varepsilon}\frac{\partial F_z}{\partial y} = \frac{\beta_y}{\varepsilon} A_{mn} cos(\beta_x x) sin(\beta_y y)[C_3 cos(\beta_z z) + D_3 sin(\beta_z z)] \tag{4.18}$$

Applying the boundary condition in (4.17) it is shown that

$$\begin{aligned} E_x(0 \le x \le a, 0 \le y \le b, z = 0) &= \frac{\beta_y}{\varepsilon} A_{mn} cos(\beta_x x) sin(\beta_y y)[C_3(1) + D_3(0)] = 0 \\ &\rightarrow C_3 = 0 \end{aligned} \tag{4.19}$$

$$\begin{aligned} E_x(0 \le x \le a, 0 \le y \le b, z = c) &= \frac{\beta_y}{\varepsilon} A_{mn} cos(\beta_x x) sin(\beta_y y) D_3 sin(\beta_z c) = 0 \\ &\rightarrow sin(\beta_z c) = 0 \rightarrow \beta_z c = sin^{-1}(0) = p\pi \\ &\rightarrow \beta_z = \frac{p\pi}{c}, \quad p = 1,2,3,... \end{aligned} \tag{4.20}$$

This reduces the expression for the potential function to

$$F_z(x,y,z) = A_{mnp} cos(\beta_x x) cos(\beta_y y) sin(\beta_z z) \tag{4.21}$$

where

$$\begin{aligned} \beta_x &= \frac{m\pi}{a}, \quad m = 0, 1, 2, ... \\ \beta_y &= \frac{n\pi}{b}, \quad m = 0, 1, 2, ... \\ \beta_z &= \frac{p\pi}{c}, \quad m = 0, 1, 2, ... \end{aligned} \tag{4.22}$$

m and n not both 0 simultaneously

All of the electric and magnetic field components can be found in appendix A. Now, using (4.22) the dispersion relation for the cavity mode can be expressed as

$$\beta_x^2 + \beta_y^2 + \beta_z^2 = \beta_r^2 = (2\pi f_r)^2 \mu\varepsilon \tag{4.23}$$

or

$$(f_r)_{mnp}^{TE} = \frac{1}{2\pi\sqrt{\mu\varepsilon}} \sqrt{\left(\frac{m\pi}{a}\right)^2 + \left(\frac{n\pi}{b}\right)^2 + \left(\frac{p\pi}{c}\right)^2} \quad \begin{array}{l} m = 0, 1, 2, ... \\ n = 0, 1, 2, ... \\ p = 1, 2, 3, ... \\ m \text{ and } n \text{ not both 0 simultaneously} \end{array} \tag{4.24}$$

The patch antenna can also be viewed as an open circuit stub. This means that the current at the end of the patch is zero, maximum at the center of the patch, and ideally zero at the beginning of the patch. The reflection coefficient of an open circuit is $+1$ and this means that the voltage is maximum at the edges and minimum at the center. This demonstrates why the input impedance of the patch is high since the voltage is maximum and the current is minimum. It also explains why the patch antenna radiates - the fringing fields on the edges are in the same direction and add in phase producing radiation. The currents on the patch and the ground add in phase but are in opposite directions, so they cancel each other out. Therefore the patch is a voltage radiator. This is demonstrated in figure 4.6 with an HFSS simulation where the E-field vector is plotted.

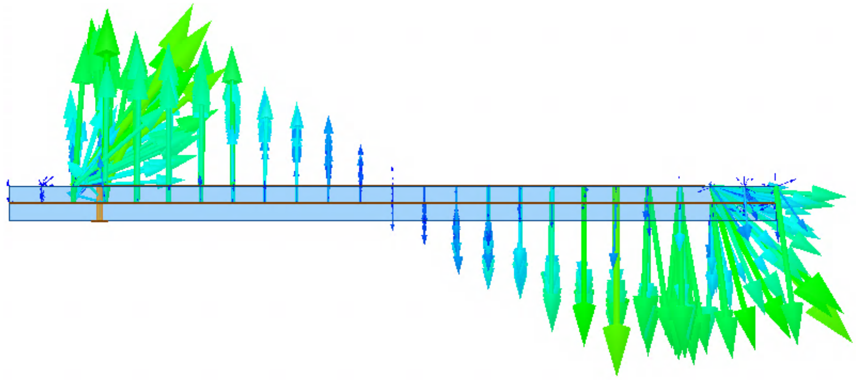

Figure 4.6: The simulated E-field distribution for the cavity mode of a patch antenna plotted in vector format in HFSS

The shorting post added in the PIFA is a physical short to ground. This replaces the virtual ground that arises in the half-wave patch antenna. Therefore, the same field distribution described in the cavity mode of the patch antenna is now valid for the PIFA. The difference is that the trailing edge (opposite the feed) is a PEC (perfect electric conductor) since it is a physical via.

The resonant frequency of the dominant mode is approximated by [46]

$$f_0 = \frac{c}{4(W+L)\sqrt{\varepsilon_r}} \tag{4.25}$$

This is a very simple equation which relates the area of the antenna to a quarter wavelength in the dielectric material. It is derived from the monopole antenna, in that the physical length of the antenna is quarter wavelength. While this equation is not very comprehensive, it can be used to begin a design. More in depth equations have been generated such as in [47], but for a PIFA that is shorted with a through-hole via it is suggest in [48] that a more realistic approximation is given by

$$f_0 = \frac{c}{4 \cdot 0.9 \cdot (W + L - \pi d)\sqrt{\varepsilon_r}} \tag{4.26}$$

where d is the diameter of the through-hole and the term 0.9 comes from calculated versus measured results done in [48].

A model of a patch with a shorting post is designed in HFSS and can be seen in figure 4.7.

The patch was put on the top layer and the feed was placed on the bottom layer with a ground layer in between. Each dielectric layer is 20mil and each copper layer is 1oz. The dielectric layers are TMM 10i with a relative permittivity of 9.8. In a patch with a single shorting post it is typically placed in the corner as to maximize the current path, as shown in figure 4.8. The feed position is chosen to minimize the input impedance to better match with the typical 50Ω. Using (4.26), for a frequency of 2.45GHz the $W + L$ is 10.8mm. This was simulated and through experimentation it was found that a $W + L$ of 11.3mm resulted in a resonant frequency of 2.45GHz. The ground plane is 20mm×20mm, which is the maximum size allowable in the specifications.

Even with the feed pin placed very close to the shorting pin, and thus minimizing the impedance, there is still a very large impedance presented by the antenna. Getting a good match with this antenna will be difficult and it is clear that efforts need to be made to reduce the input impedance. This was shown in [49] where even after trying to optimize the placement of the feed and the short a suitable input impedance match

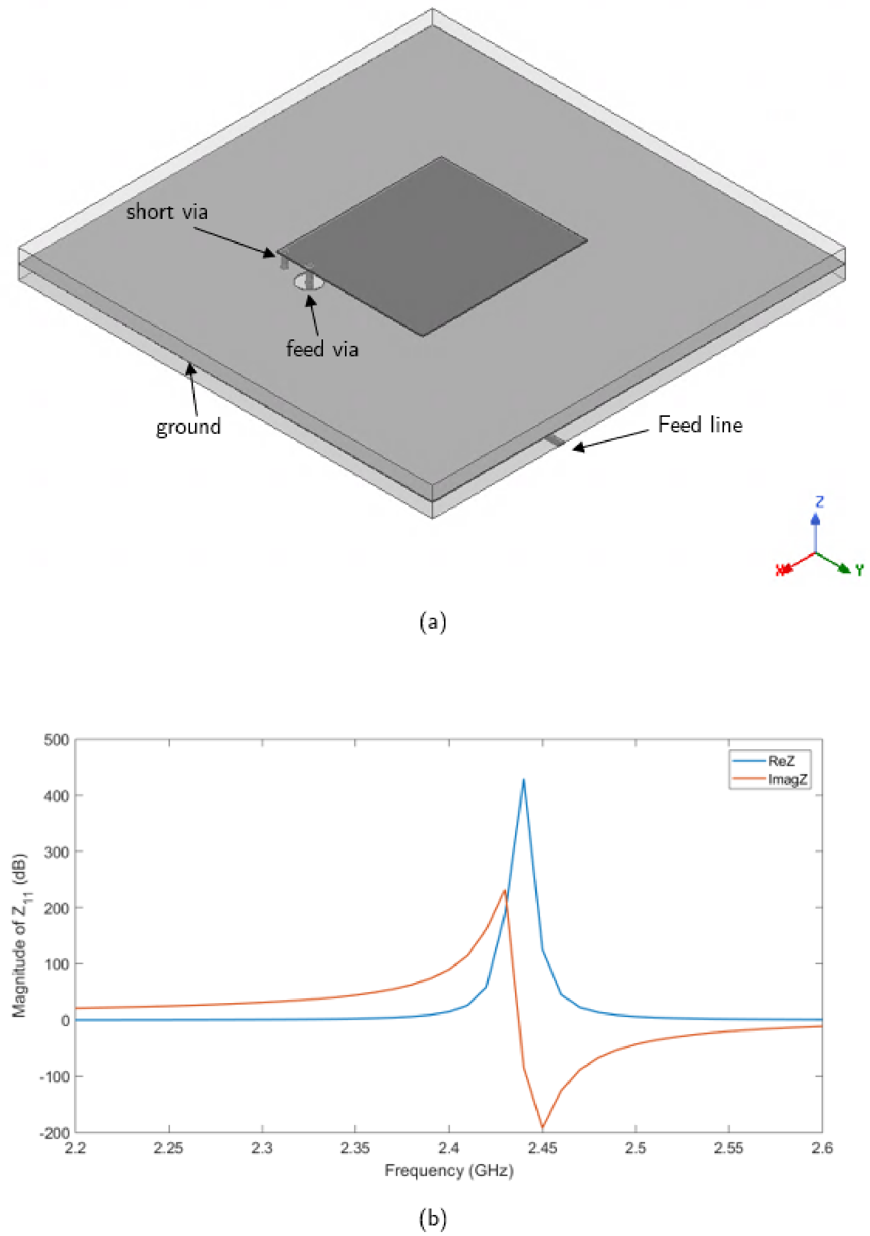

Figure 4.7: (a) HFSS model of a shorted patch with the patch, ground, feed via, short via, and dielectric visible. (b) Plot of the simulated Z parameters.

was not achievable. Slots were introduced into a regular PIFA to control the input impedance and achieve a wide reflection coefficient 10dB bandwidth.

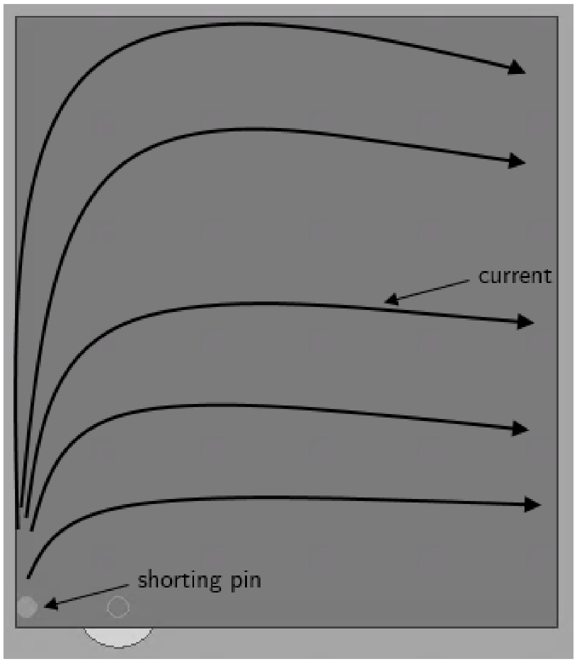

Figure 4.8: Current lines of a shorted patch antenna with a single shorting post in the corner. This shows the maximum length of the current path.

4.4 PIFA with single open circuit slot

One technique to reduce the input impedance of a PIFA is to introduce a slot into the patch. There are two types of slots that can be added: inductive and capacitive. Shown in [50], single or multiple slots can be added in order to more finely control the input impedance. This concept can also be used to create a dual-band functionality. A simple model of a PIFA with a single slot is shown in figure 4.9. The slot location impacts the path of the current and this is what can lead to the inductive or capacitive load on the input impedance. When a slot is added to the right of the feed, as in figure 4.10(a), then the current (or magnetic field) is confined to the area near the feed and inductively loads the input. In figure 4.10(b) the feed is now electrically further from the ground, raising the resistance, and the current in confined between the input and the short, which capacitively loads the input.

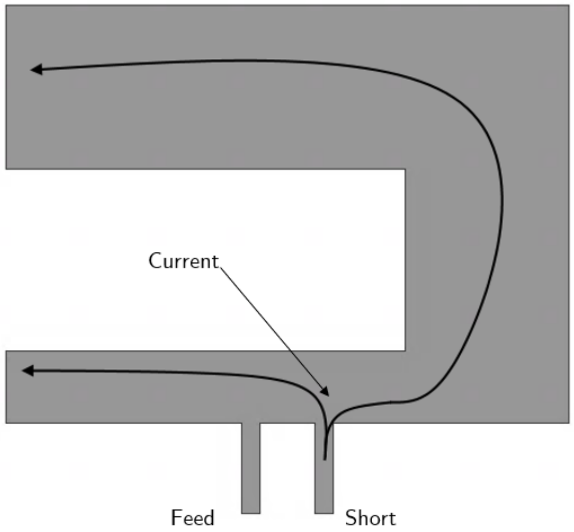

Figure 4.9: PIFA with a single slot showing the two paths of current and the dual-band functionality this creates.

The slot location impacts the path of the current and this is what can lead to the inductive or capacitive load on the input impedance. When a slot is added to the right of the feed, as in figure 4.10(a), then the current (or magnetic field) is confined to the area near the feed and inductively loads the input. In figure 4.10(b) the feed is now electrically further from the ground, raising the resistance, and the current is confined between the input and the short, which capacitively loads the input.

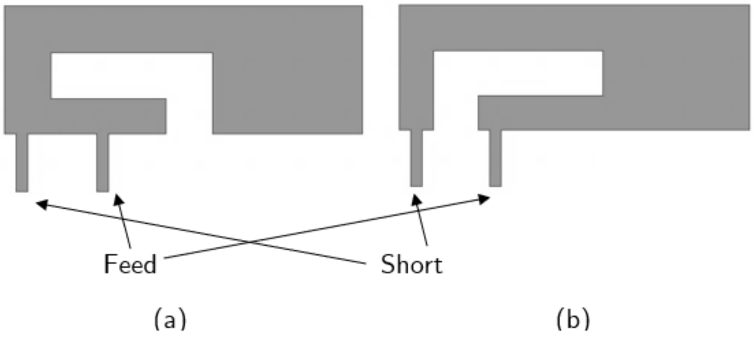

Figure 4.10: PIFA with (a) inductive tuning slot and (b) capacitive tuning slot added.

4.5 PIFA with U-shaped Slot

Similar to the open circuit slot, a U-shaped slot can be added to a PIFA to create a dual-band functionality, as well as tune the input impedance. Presented in [46, 51, 52, 53], a slot with the length and width of a second resonance is added into the patch which can be seen in figure 4.11.

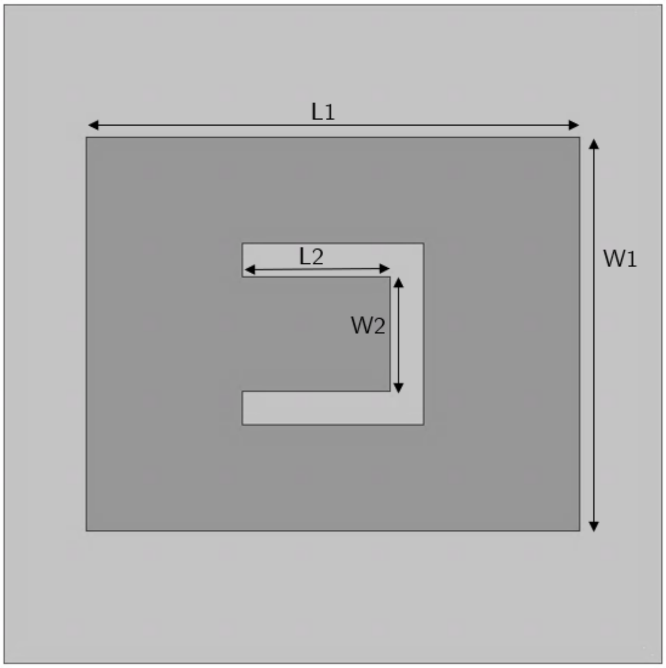

Figure 4.11: PIFA with a U-shaped slot that adds dual band functionality.

The parameters L1 and W1 refer to the lengths and widths of the lower resonance and the parameters L2 and W2 refer to the lengths and widths of the higher resonance. These are calculated using 4.26 much like a regular PIFA. The difference is that tuning of the input impedance has more degrees of freedom with the gap width of the slot and the placement of the slot playing a factor. It was shown in [53] that the outer dimensions, L1 and W1, only affect the lower resonance and not the upper resonance, while the opposite is true for the inner dimensions. The width of the U slot affects the VSWR bandwidth of both frequencies and moving the placement of the slot can shift the resonant frequency and the input impedance.

4.6 Effect of High Permittivity Materials on PIFAs

As discussed in section 4.3, high permittivity substrates can be used to miniaturize an antenna, at the cost of performance. Shown specifically for PIFAs in [54], the use of high permittivity materials can severely impact the performance of the antenna. It was shown that on an alumina substrate, with relative permittivity $\varepsilon = 9.4$, a percent bandwidth of 0.5% is achieved. Another substrate, Roger 3210 ($\varepsilon = 10.2$), was also used and this was able to achieve a percent bandwidth of 0.2%. Overall, the bandwidth decreases as the relative permittivity increases. The two materials also showed a very low gain because of the high loss compared to the other materials used in the test. When the $tan\delta$ was set to 0 very high gain was achieved. Therefore, the high permittivity can help gain if the material has a very low loss.

4.7 Effect of Ground Plane Size on Radiation Performance

The effect of the size of the antenna compared to the size of the ground plane is considered in [55]. A patch antenna was designed in HFSS and the length that the ground plane extended past the patch was varied. It was found that when the length that the ground extended past the antenna was minimum, that the 3dB bandwidth of directivity was therefore maximum. A wide beam is desirable in this application because the specimen is moving around the enclosure. Ergo, a ground plane that extends as little as possible past the antenna is advantageous.

CHAPTER 5: DESIGN AND SIMULATION OF PROPOSED ANTENNA

The background and theory discussed previously is now implemented to design a shorted microstrip patch antenna with a single open slot. This antenna is designed to operate in the ISM 2.4GHz band and is initially designed to operate at a center frequency of 2.45GHz. The antenna design is truly that of a dual band PIFA, where the fundamental resonance is at 725MHz and the second resonance is at 2.5GHz. A slot is inserted into the antenna to reduce and control the impedance at the second resonance. A single band PIFA that has a fundamental resonance at 2.45GHz would offer a smaller design, but the larger antenna has its benefits. Because there will need to be electronics on the design as well, the ground plane will need to remain relatively large to accompany the SMD components. The larger antenna size, for a fixed ground plane, helps to widen the beam. A wide beam is necessary for the implanted antenna because the host is roaming around. Having a wider beam enables the receive antenna to in the telemetry link to connect to the implant over the area of the enclosure better. If the ground plane was much larger than the antenna then it would serve to reflect more energy and reduce the beam width, as shown in section 4.7.

5.1 Proposed Antenna Design

5.1.1 Material Selection

To begin the design some initial specifications need to be decided. The dielectric material used in the design will be the Rogers Tmm 10i laminate. This material is chosen for its very high relative permittivity, it can be made very thin (20mil), it is designed for microstrip and stripline applications, has very low thermal coefficient of dielectric constant, and is relatively low loss. The high relative permittivity enables the design to be electrically small and helps the antenna interface with the insulating material. The insulation material has a relative permittivity of 9.4 and the dielectric has a permittivity of 9.8. Although the high dielectric constant will create more coupling inside the material and reduce the radiation away from the antenna, the high dielectric constant is necessary to achieve the physical size. The loss tangent in HFSS is given as 0.002. Material parameters for the the Tmm 10i laminate are given in table 5.1.

Table 5.1: Material parameters for the Rogers Tmm 10i laminate [2].

Electrical Properties				
Dielectric Constant (process)	Dielectric Constant (design)	Thermal Coefficient of Dielectric Constant	Volume Resistivity	Electrical Strength
9.80 ± 0.245	9.9	-43 (ppm/K)	2×10^8 (MΩ·cm)	267 (V/mil)

The dielectric thickness that will be used is 20mil. This thickness is chosen to keep the microstrip lines small. A thin dielectric is also good for radiation purposes in that a broader radiation pattern can be achieved. The conductor is a 1oz copper (0.035mm) on the dielectric.

The insulation layer is made from alumina, as discussed in section 3.4. Alumina is chosen for its high bio-compatibility, its excellent heat performance, and its low electrical conductivity. The insulation layer is necessary to protect the tissue from the electrical components and to simultaneously protect the electrical components from the lossy tissues. The choice of alumina will degrade the performance of the antenna, but the insulation is paramount.

5.1.2 Design Specifications and Parameters

The design begins in the HFSS simulation software and the final design is shown in figure 5.1.

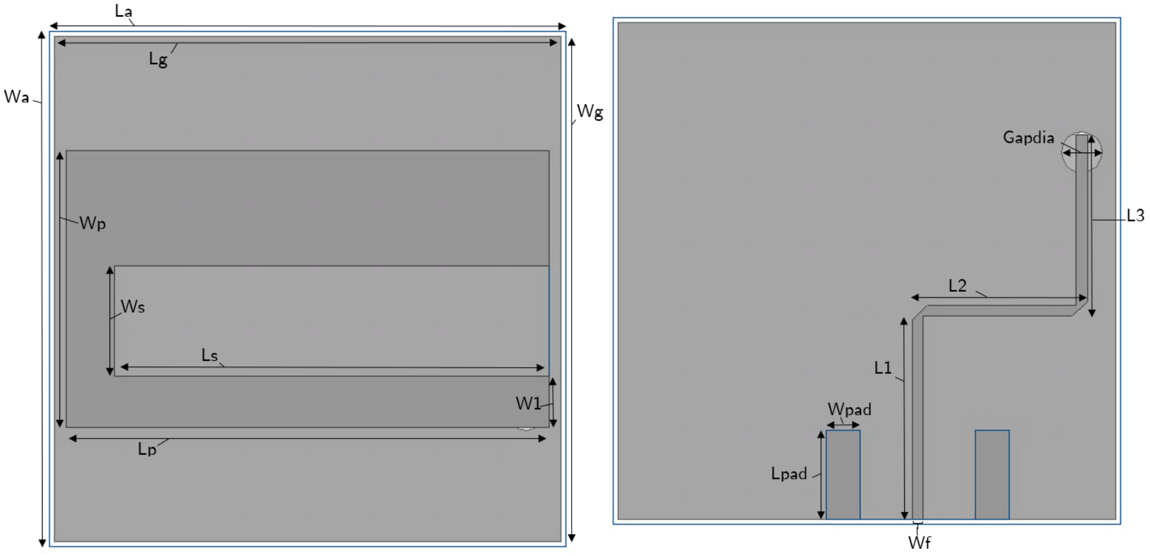

(a) (b)

Figure 5.1: (a) Top and (b) bottom views of the final PIFA design modeled in HFSS with relevant measurements marked.

The terms La and Wa refer to the length and width of the insulating layer. The height of the insulating layer in the final design is a total of 5.5mm. This leaves 2.17mm above the radiator and 2.24mm below the bottom trace. In order to leave space for the feed via, a portion of the ground plane is taken out, a circle with diameter Gapdia. Pads, shorted to ground, were placed on the bottom layer so that an SMA connector could be soldered onto the design for testing. The width of the feed, which becomes a buried microstrip line when the antenna is loaded with the insulating layer, results in an impedance of 49Ω. There is a feed via that connects the bottom trace to the antenna on the top layer, as well as a shorting via that connects the antenna to ground, both 0.2mm in radius. The vias are shown in figure 5.2.

Figure 5.2: Vias shown in the final design.

The dimensions marked in figures 5.1 and 5.2 are given in table 5.2. This is the final design for the purpose of this thesis. For the true final design that will be integrated with the entire WBAN the SMA pads would not be in the design. Additional layers, as well as components, would be added on the back layer when the design is integrated with electronics.

Table 5.2: Dimensions for the final PIFA design.

Dimension	**Value** (mm)
Lp	21
Wp	12
Lg	22
Wg	22
Ls	18.9
Ws	4.8
Wf	0.3
W1	2.2
La	22.4
Wa	22.4
Gapdia	1.8
L1	9.5
L2	7.75
L3	8
Lpad	3.95
Wpad	2.5
Fx	0.75
Fy	0.5
Sx	0.25
Sy	0.5

5.1.3 Final Design Performance

The implanted radiation performance of the final design is now presented. The reflection coefficient and the 10dB bandwidth of the design is shown in figure 5.3. The achieved bandwidth of the device is 10MHz, which is in line with the information in section 4.6. While this is a meager 0.4% bandwidth, this is preferable because it reduces the need for extensive filtering when eternal electronics are added. This is also more than enough bandwidth to send the signals captured from the brain probes, even at the maximum data rate described in section 1.2.1.

The directivity of the antenna, as well as the beamwidth, is shown in figure 5.4.

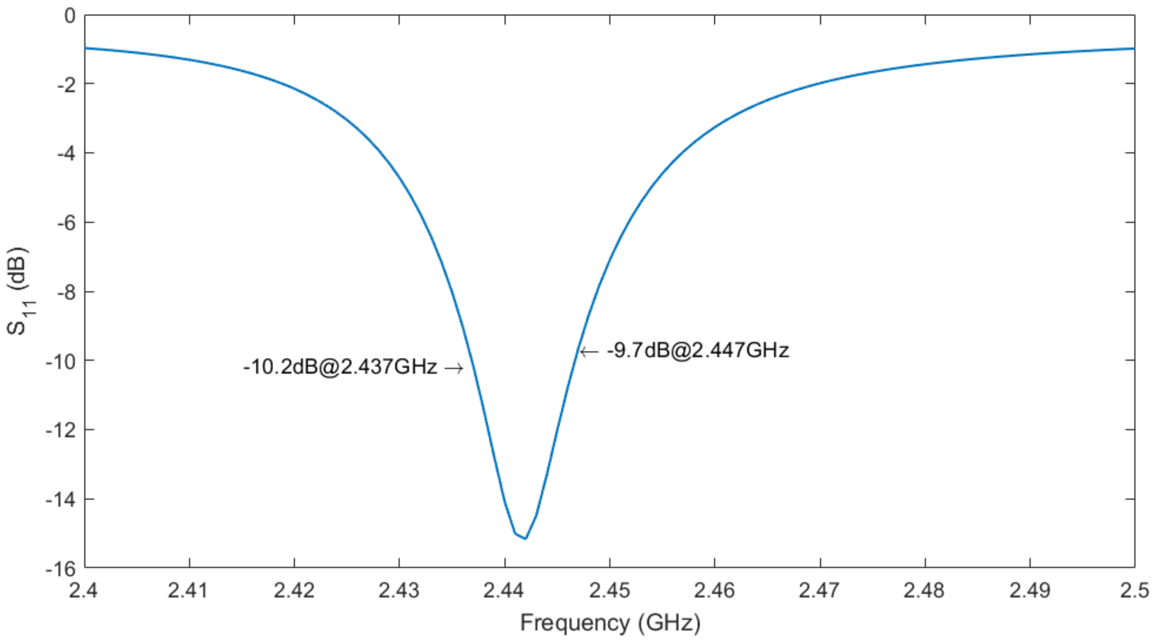

Figure 5.3: Reflection coefficient of the final design as simulated in HFSS.

Directivity is taken at two planes along the antenna: the $\phi = 0°$ and the $\phi = 90°$ plane. Beam width is calculated by taking the 3dB width of each of these planes. Maximum directivity in the 0° and 90° planes is 5.22dBi and 5.16dBi respectively. The 3dB beamwidth is 119°and 128° in the 0° and 90° planes respectively. It is also important to note that the directivity in the reverse directions is very low, peaking around -2dB. The reverse directions are those that point towards the rat's brain and it is desirable to have as little energy as possible in those directions.

A comparison of the antenna designed in this work with those designed in other works is given in table 5.3.

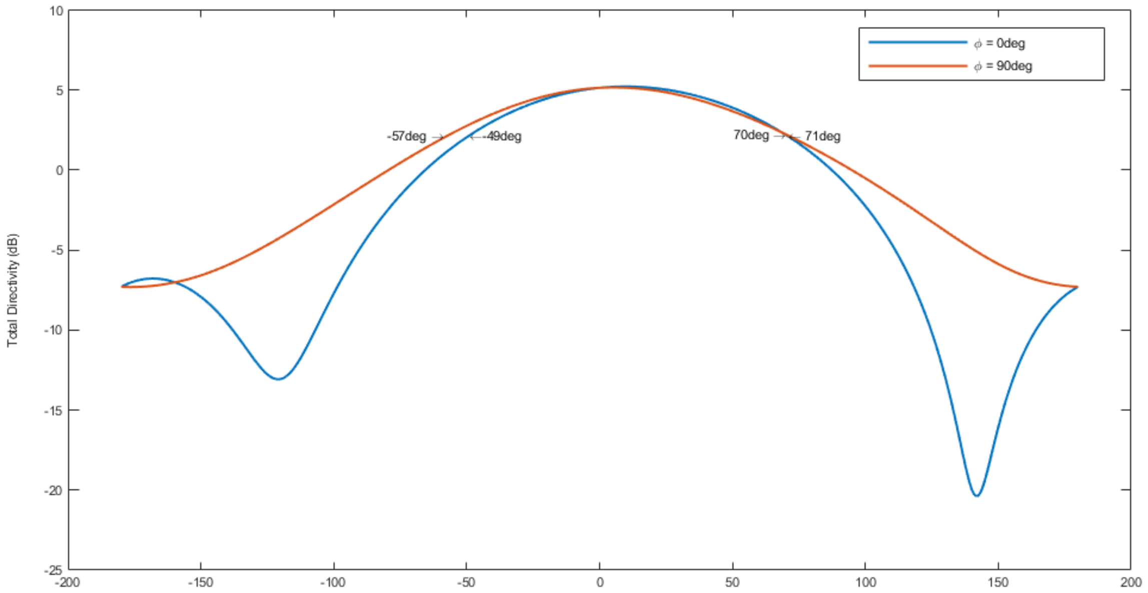

Figure 5.4: Total directivity of the final design as simulated in HFSS.

Table 5.3: Comparison of performance with selected works.

Reference	**Antenna Type**	**Operating Frequency**	**Size** (mm^2)	%**BW**	**Max directivity** (dBi)	**Beam width** (degrees)
[56]	PIFA	ISM	54.35	8.1	2.91	124.5
[57]	PIFA	MICS	156.25	2.2	1.65	97.6
[58]	PIFA	MICS/ISM	200	13.9/8.2	–	–
[59]	PIFA	MICS	488	1.7	2.61	252
This work	PIFA	ISM	484	0.4	5.2	128

5.2 PIFA in Tissue Phantoms

5.2.1 Tissue Variations

To account for the tissue that the antenna will be implanted in, tissue phantoms were created in HFSS using data from section 3.2.1. The values used for the permittivity and conductivity for each tissue are listed in table 5.4.

Because the implant will be in the rat's skull, the thickness of the skull, skin, and

Table 5.4: Tissue parameters used in the final design.

Tissue	**Permittivity** (ϵ_r)	**Conductivity** (σ)	**tanδ**
Skin	31	1.04	0.14
Bone	18	0.53	0.12
Brain	45	1.33	0.12

muscle need to be investigated. According to [60, 61] the thickness of the skin ranges from 0.5mm to around 1mm. The mean thickness of a rat skull was found to be 0.7mm in [62], but could range from 0.5mm to 1mm as well. Assuming that the implant will not be in the brain, but can extend all the way through the skull, simulations were run at the edge cases. The tissue phantoms extended 4.8mm away from the edges of the insulating layer. Figure 5.5 shows the model setup in HFSS. Thickness of 0.5mm and 1mm were then used for each layer to understand the effect that the changing thickness might have on the implant. Each simulation was done with the implant at full depth, or adjacent to the brain phantom. The brain phantom extends 4mm below the insulation. Losses were used in the phantoms for these simulations.

As it can be seen in figure 5.6 the implant is invariant to the thickness of the tissue. The insulation layer, while providing its own dielectric loading effect, shields the antenna from the more serious effect of the lossy tissue. The tissue thicknesses are very small and the insulation layer is very thick, which exemplifies the need for the insulation layer.

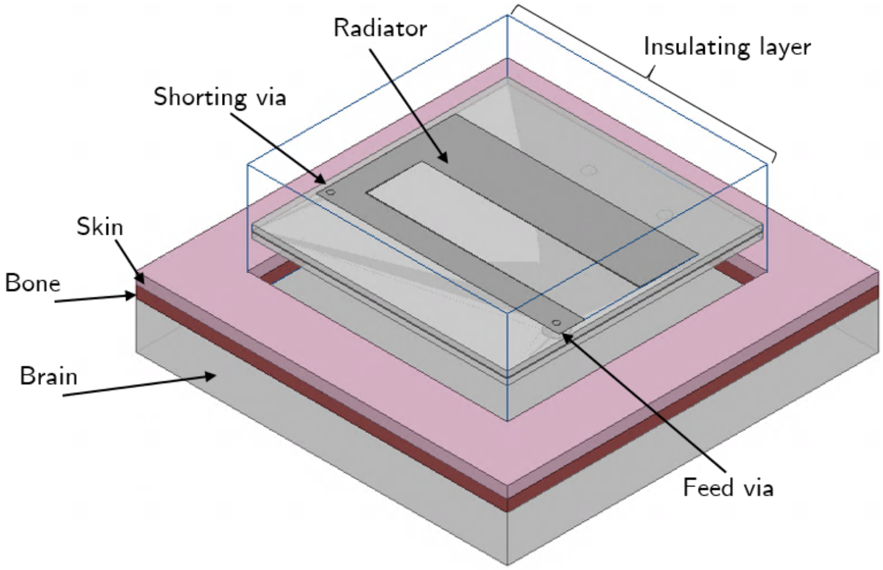

Figure 5.5: HFSS model used for varying the thickness of the skin and bone phantoms.

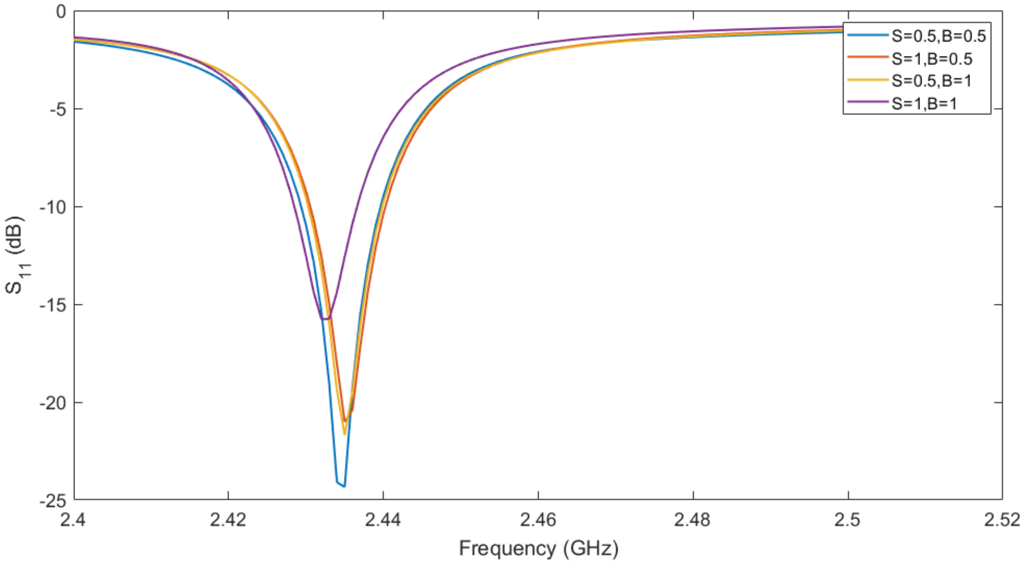

Figure 5.6: The reflection coefficient seen when varying the thickness of the skin and the bone phantoms to account of variation in actual rat tissue.

5.2.2 Simulated Specific Absorption Rate

In order to verify if the antenna is safe to implant in biological tissue the SAR is calculated. The limit for SAR, as mentioned in section 1.2, is 1.6W/kg in a 1g averaged mass. HFSS has a built in calculation for SAR that uses IEEE Standard P 1528.4 to calculate it. The calculation takes into account the mass density of the material that is defined, the averaging weight (in this case 1g), and a voxel size. The equation used to calculate the average SAR is shown in (2.21). The program then divides the tissue into voxels, which is a 3-dimensional object, and calculates the average SAR in that volume. The mass density of the three tissues used is laid out in table 5.5. Typical mass densities for organs is around 1(g/cm^3), whereas bone is much more dense.

Table 5.5: Mass density used in HFSS for the tissues present in a rat [3].

Tissue	**Mass Density** (g/cm^3)
Skin	1
Bone	1.2
Brain	1.05

The input power to the antenna was then varied to determine when the SAR in the tissues exceeded the recommended safe limit. It was found that an input power value of 8.5mW (9.29dBm) produced a peak average SAR of 1.54W/kg in the brain tissue. The SAR measured in the bone and the skin is lower due to the lower conductivity in those tissues. The maximum output of the Texas Instruments CC2543 SOC (system on chip) is 5dBm, which is equivalent to 3.16mW. The simulation was also run with this input power to calculate the maximum SAR that the antenna would output in the proposed system. The following figures depict the tissues and their calculated SAR at the two input power levels.

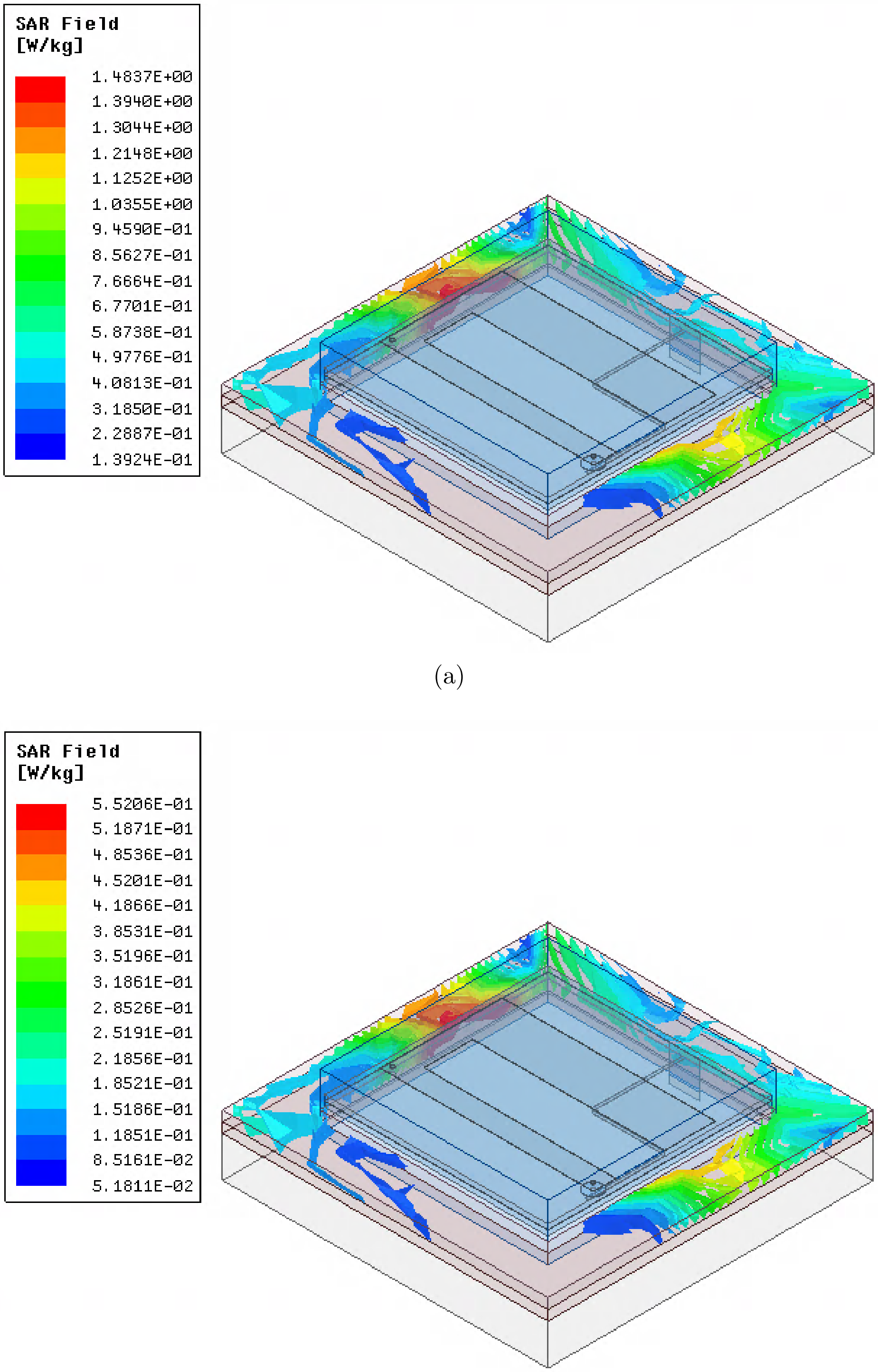

(a)

(b)

Figure 5.7: SAR as calculated by HFSS in skin tissue with (a) 8.5mW input power and (b) 3.16mW input power.

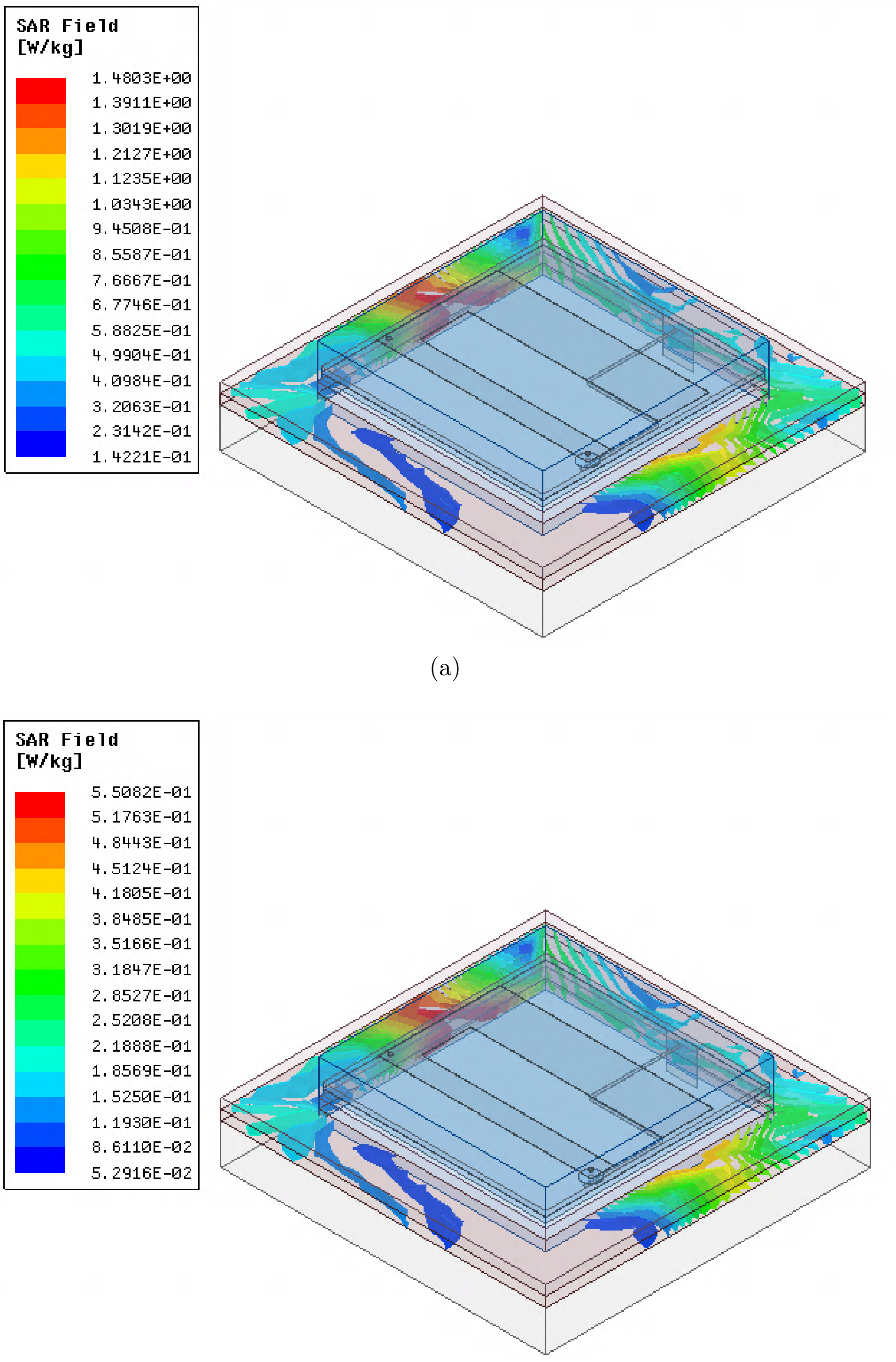

(a)

(b)

Figure 5.8: SAR as calculated by HFSS in bone tissue with (a) 8.5mW input power and (b) 3.16mW input power.

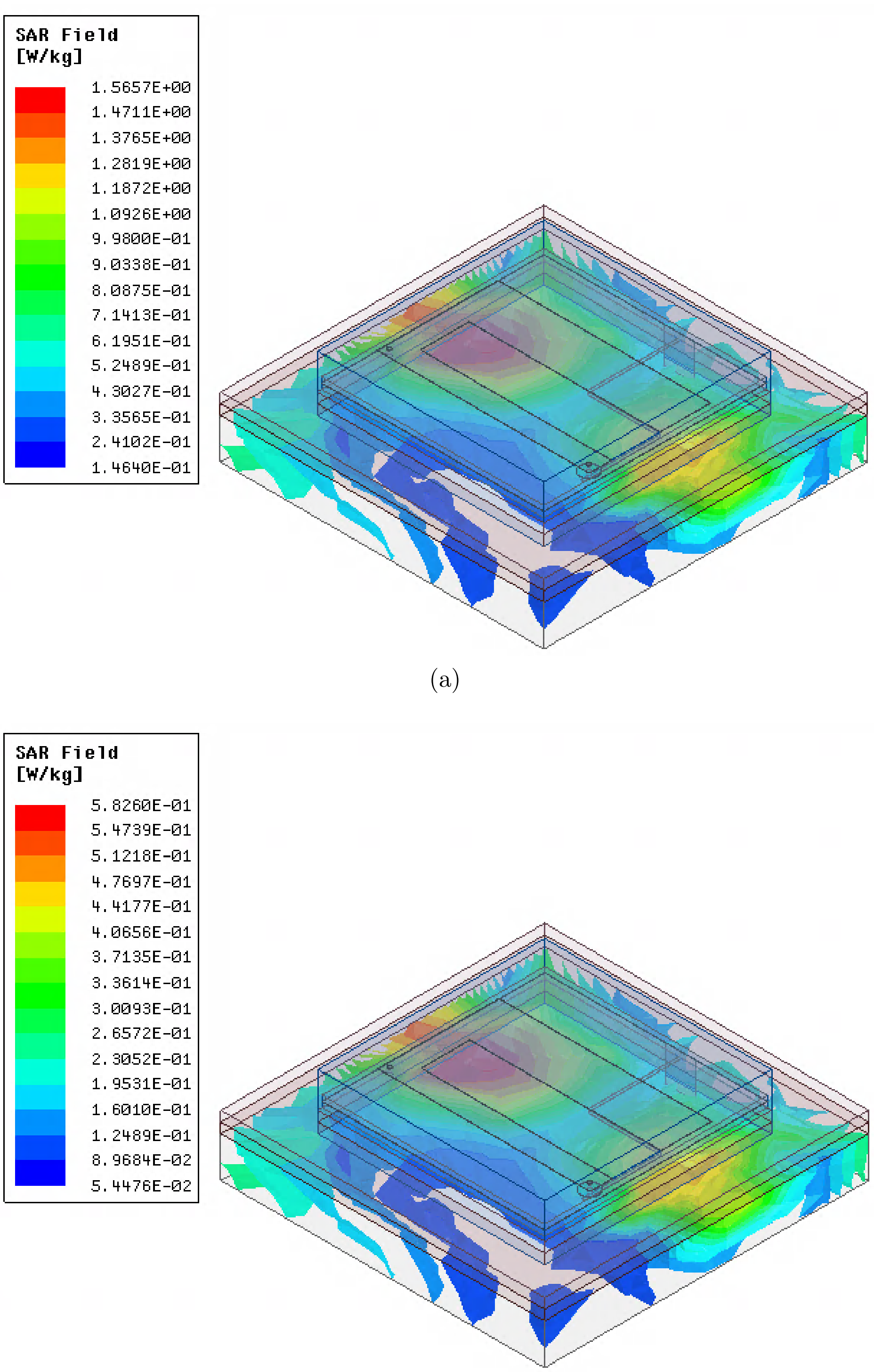

(a)

(b)

Figure 5.9: SAR as calculated by HFSS in brain tissue with (a) 8.5mW input power and (b) 3.16mW input power.

As it was shown in figure 5.9b, the maximum SAR that is calculated is 0.583W/kg in brain tissue with a 3.16mW input power. Therefore, even with the maximum output power available from the SOC, the antenna is well within safe limits for the surrounding tissue.

CHAPTER 6: RF COMMUNICATION SYSTEM

The implant for the WBAN is not complete until there is a communication system present to interface the electrode grid with the antenna. For this implant the data is coming from a grid of 32 electrodes placed on the brain similar to the one shown in [63].

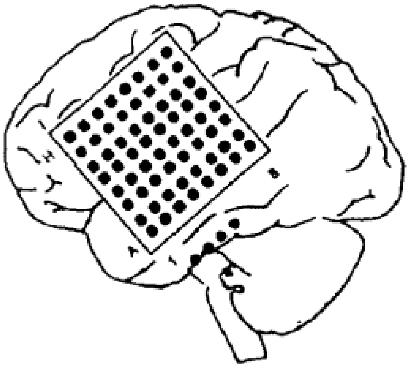

Figure 6.1: Electrode grid placed on the brain to collect the iEEG signals [63].

The voltage signals coming from the electrode grid are random signals that can vary between 10Hz to 7kHz and have very small amplitudes. These signals will need to be processed in order to be sent over the wireless telemetry link. In its simplest form, the communication system will feature a low noise amplifier, a modulator, and a filter.

Because the amplitudes of the brain signals are so small the amplifier is needed to take those signals to a usable level for transmission. The mixer would mix the signals up to the 2.4GHz ISM band for transmit through the antenna, with the high

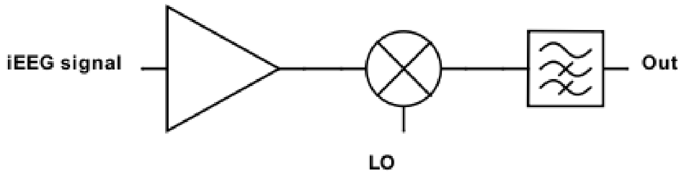

Figure 6.2: Block diagram of the communication system for taking the brain signals to the antenna.

frequency signal coming from a local oscillator (LO). The high pass filter allows the high frequency signals to pass and blocks any DC biasing for the amplifier and low frequency noise in the circuit. The signals are then sent over the wireless telemetry link where, at the base station, the signals can go through a seizure detection algorithm for further study. This is discussed in [64], where a similar system is shown and a seizure detection algorithm is presented. Because none of the processing needs to be done on the implant itself, the circuitry can be minimal and all the processing can take place at the base station.

6.1 Components for Communication System

Off the shelf components may be used to achieve the communication system for a relatively low cost. While these components may be cost effective, they are usually not designed for extremely specific applications and may take up extra space. Intan technologies manufactures the RHD2000 series of integrated circuits that is designed for neural recording. The RHD2132 is a digital elecrophysiology interface chip that features 32 input channels with fixed gain amplifiers that feed into an analog multiplexer that is then digitized through a single ADC. This chip has fixed gain amplifiers that produce sufficient gain for the low amplitude brain signals without boosting the signals high enough such that the ADC cannot resolve the voltage steps [65]. A simplified block diagram of the RHD2132 can be seen in figure 6.3.

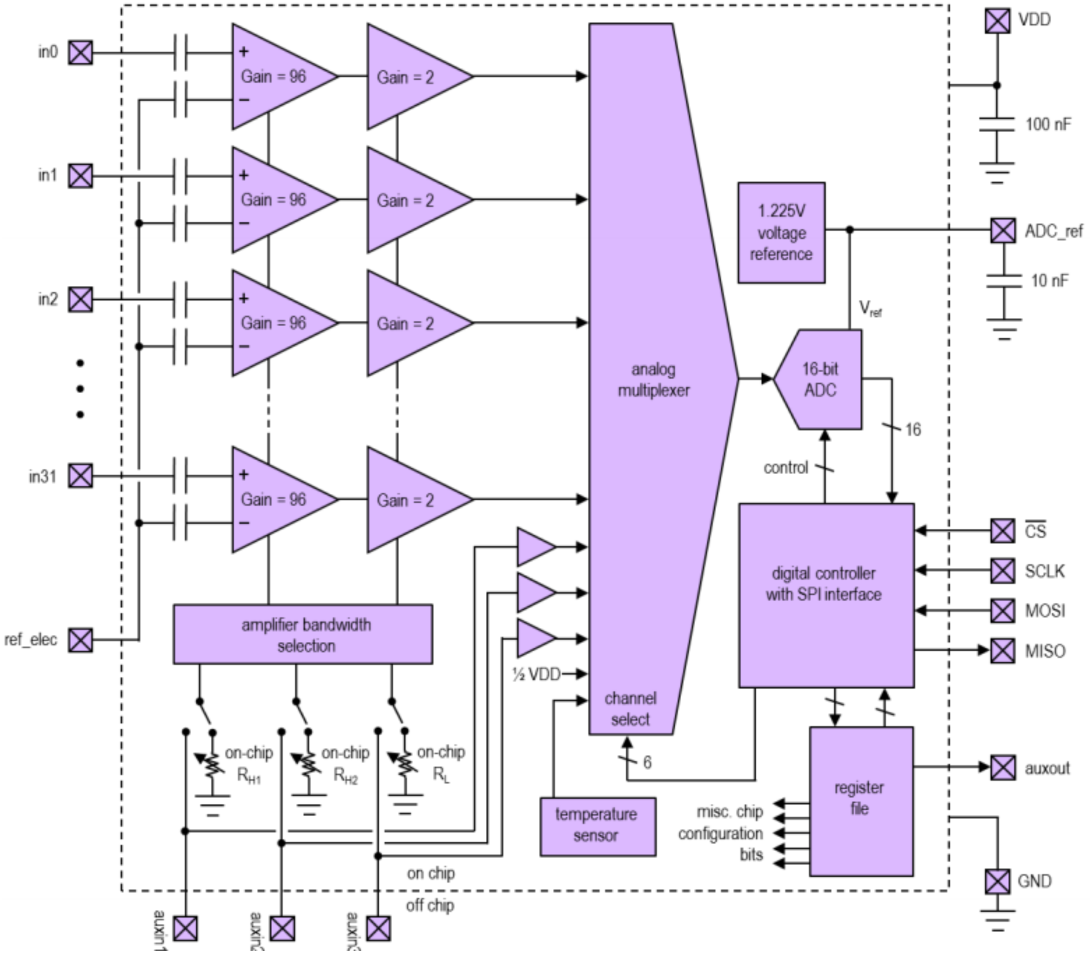

Figure 6.3: Block diagram of the Intan RHD2132.

The output of the RHD2132 is a low voltage differential signaling (LVDS) serial peripheral interface (SPI), which interfaces well with other digital chips on the same board. This means that the chip select, clock, and master-out slave-in (MOSI) pins are are differential and communicates with a voltage difference between two wires. Amplifier bandwidth can be easily controlled through programming of on-chip resistors or with off-chip resistors. The ADC in the chip has a maximum sample rate of 30k samples/s. This can be adjusted lower for a loss of accuracy, but a gain in bandwidth. The low frequency signals that this chip is digitizing should only need sampling on the order of 1k sample/s, so the ADCs in the chip are more than adequate. The total package size of the chip is 8mmx8mm and does not need many off chip components. While, this chip can take the low voltage signals from the brain, amplify them, and ultimately digitize them, they are not able to be sent directly to the antenna for transmission.

The Texas Instruments CC2543 system-on-chip (SoC) is a fully featured single chip transceiver and micro-controller unit (MCU). This chip has the ability to interface with SPI, has a programmable frequency output in 1MHz steps, is low power, and comes in a 5mmx5mm package size. The CC2543 is able to take the digital signals from the RHD2132 as an input and is able to mix them up to the required frequency in the 2.4GHz ISM band. Because this is an SoC, it features an MCU with 1KB of random access memory (RAM) that can be used to store brain signals over time and send the packet as a burst signal so that the system is not functioning at all times, saving power and reducing heat. In transmit (Tx) mode, the CC2543 uses a mere 26mA of current at a transmit power of 0dBm (1mW). Because the brain signals are not constant, and they are so low in bandwidth, they can be stored in RAM for some time, the power usage and heat generation can be kept at a minimum. The SoC also features a very intuitive software called SmartRF Studio. This allows the chip to be programmed easily from a Windows based computer. The maximum data rate of the SoC is 2Mbps (with GFSK modulaton), which falls just shy of the 2.05Mbps maximum data rate, but that is with a sample rat of 4kbps. The low frequency signals could be sampled at a lower rate and the data could still be captured, provided it is still sampled above the Nyquist rate. The modulation also allows for the signals to fit within the 10MHz bandwidth of the antenna - the actual output of the chip is a 1MHz bandwidth signal that can be centered in steps of 1MHz.

The two chips were placed into a schematic with corresponding SMD components for external matching. The entire schematic of the system is done in Eagle and is presented in figure 6.4. The bill of materials for the schematic is detailed in appendix B. The schematic is adapted from the reference designs given by the manufacturers for both chips. There are 32 pads for soldering the electrodes that will serve as inputs to the RHD2132. The SPI pins on the RHD2132 are wired to the first port of the CC2543, which can be programmed and controlled with the MCU. A balun is built from the the reference design that matches the RF outputs on the CC2543 to a single ended 50Ω antenna.

Because the designed antenna is a microstrip antenna, the board can be a six layer PCB where there is three signal layers, two ground layers, and a power layer. The bottom four layers, which contain the routing for the antenna feed, the power plane, the ground for the components, and the component routing are detailed in figure 6.5.

The stackup for the board, shown in the design rule check (DRC) is shown in figure 6.6. In this PCB design all the routing is done on the top layer. There is a ground pour on the top layer and this is shorted to the ground layer to ensure a good ground connection across the board. The power layer is simply connected to the VDD pins on the components and there are decoupling capacitors at the pins.

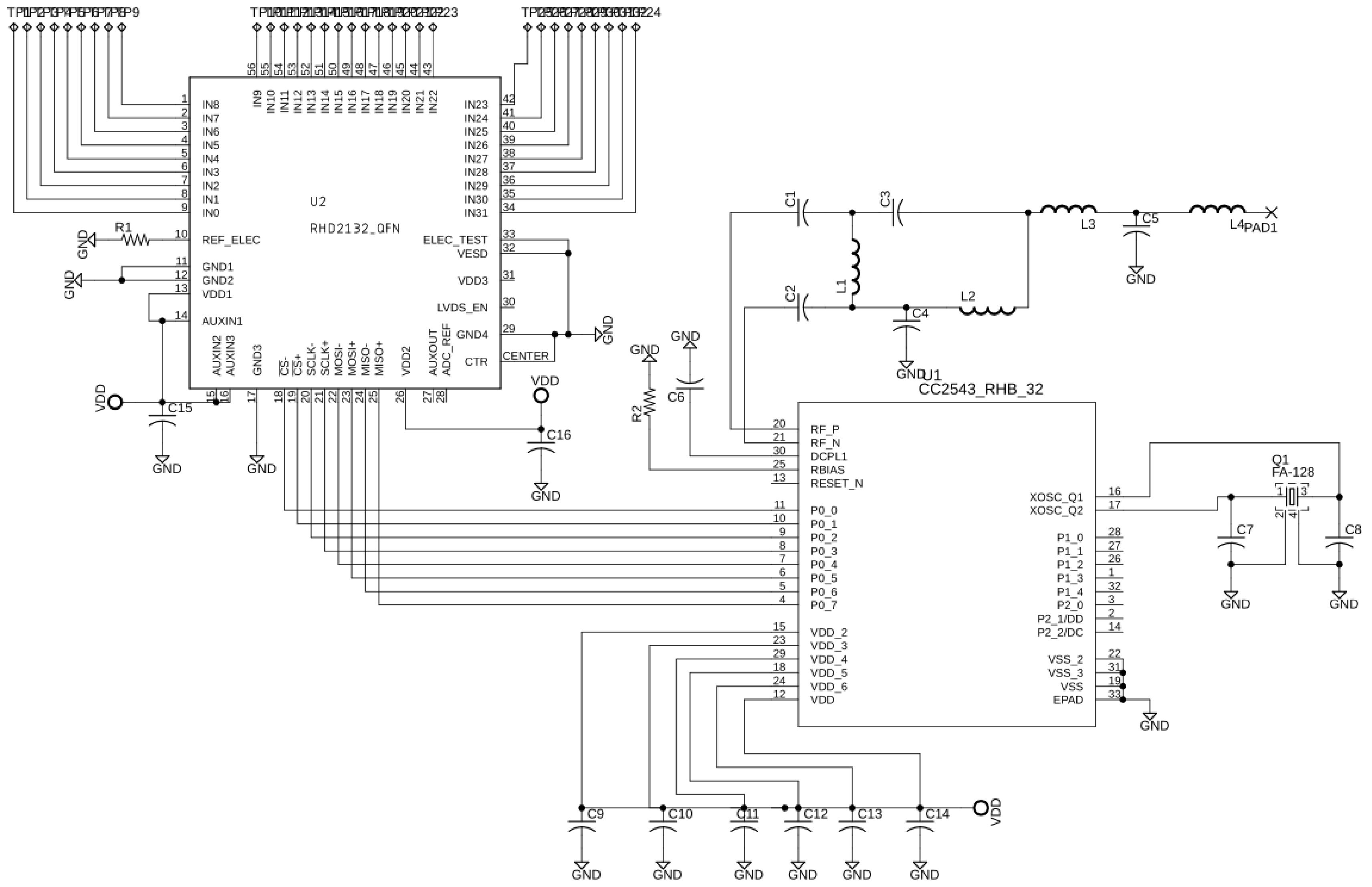

Figure 6.4: Schematic of the communication system designed in Eagle PCB software.

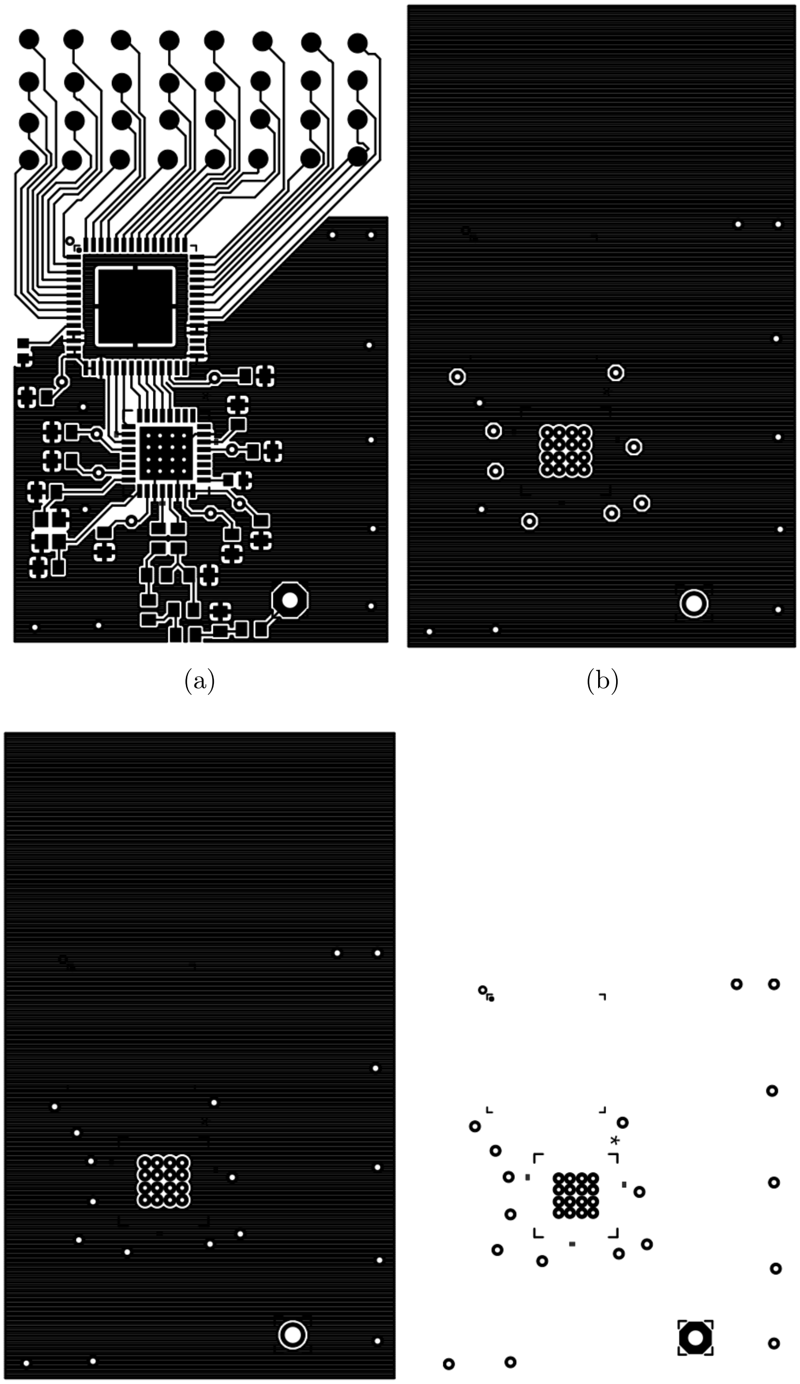
(a) (b) (c) (d)

Figure 6.5: The four layers of the designed PCB where (a) is the top, (b) is the ground, (c) is the power, and (d) is the bottom layer.

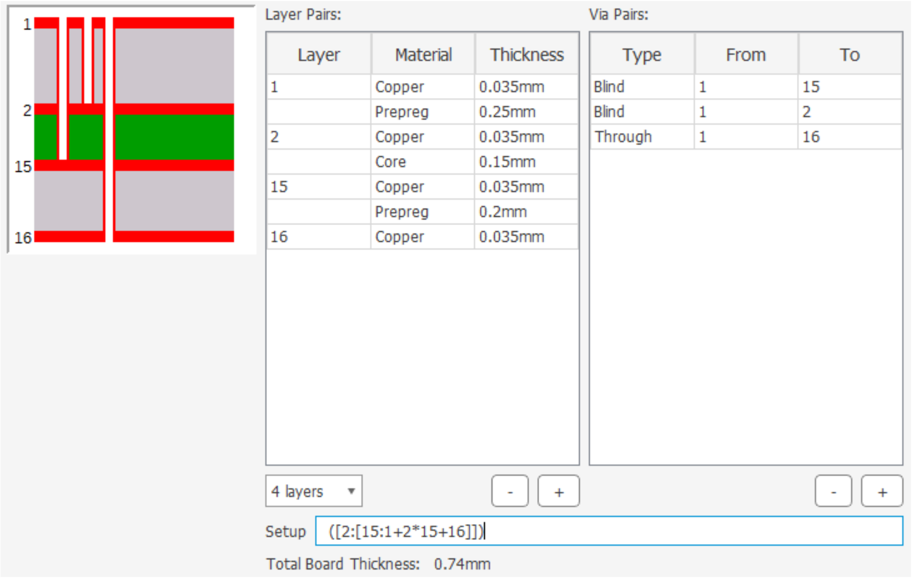

Layer Pairs:

Layer	Material	Thickness
1	Copper	0.035mm
	Prepreg	0.25mm
2	Copper	0.035mm
	Core	0.15mm
15	Copper	0.035mm
	Prepreg	0.2mm
16	Copper	0.035mm

Via Pairs:

Type	From	To
Blind	1	15
Blind	1	2
Through	1	16

Setup ([2:[15:1+2*15+16]])

Total Board Thickness: 0.74mm

Figure 6.6: Layer stackup for the PCB as shown in the DRC.

This was left with no routing and a power supply can be added, like the one mentioned in section 1.1. The bottom layer also does not have routing and is intended for the routing to the antenna feed. The overall dimensions of the PCB are 46.7x26.7mm, which is significantly bigger than the dimensions of the designed antenna. The antenna placement would determine the routing needed on the bottom later. The thickness of the board is 0.74mm, which, along with the thickness of the components, will add 1.75mm to the overall thickness of the implant.

CHAPTER 7: CONCLUSIONS

7.1 Antenna Performance

In table 1.2 a summary of the specifications needing to be met were laid out for completion of this work. Starting with the first reference, S01, with the careful consideration of biological tissue and the phantoms created in simulation, the implant meets the SAR specifications and bio-compatibility needed to be implantable. The bio-compatibility of the implant also meets the specifications for S03. The insulation layer that provides the bio-compatibility also provides an excellent life span and meets the specification for S05 as well.

The second reference, S02, is where the design falls short of the necessary specifications. The final size of the implant is 2.2x2.2x5mm^2, which is bigger than the maximum volume. The antenna presented in this work is large because of the use of the second resonance. While, it was shown that this can improve the beamwidth of the antenna, a smaller design may be necessary for the design to be implantable.

For S04, the frequency of operation, the designed antenna does operate within the 2.4GHz ISM band and has a bandwidth that supports the maximum data rate of signals produced by the brain.

7.2 Future Work

The complete synthesis of the WBAN includes fabrication and miniaturization of the components discussed in this thesis. Fabrication and testing needs to be performed in order to optimize design for necessary design tolerances and simulation error. The antenna, as well as the tissue, and entire PCB, should be fabricated to be tested against the simulation. Fluid can be made with tuned dielectric parameters that can emulate those of biological tissue. This will validate the dielectric effects that the tissue presented in HFSS.

The communication system, while functional, would benefit from being custom designed rather than off the shelf. The components selected are rather bulky and may have features or components that are not salient to this application. An all in one chip with carefully selected features would have a lower power consumption and parameters specifically tuned for the task at hand. A custom made part, even with additional SMD components, and solder pads for the electrodes could probably be made to fit on the bottom plane of the antenna.

The power supply needs to be incorporated into the implant as well. Because the implant should be battery-free, the wireless power supply needs to be added to interface with the power plane in the PCB.

REFERENCES

[1] (accessed 2018) Ism-band and short range device regulatory compliance overview. [Online]. Available: http://www.ti.com/lit/an/swra048/swra048.pdf

[2] (accessed 2018) Thermoset microwave materials data sheet. [Online]. Available: https://www.rogerscorp.com/documents/728/acs/TMM-Thermoset-Laminate-Data-Sheet-TMM3-TMM4-TMM6-TMM10-TMM10i-TMM13i.pdf

[3] W. Miller, C. Siantar, D. Fisher, M.-A. Descalle, T. Daly, J. Lehmann, M. Lewis, T. Hoffman, J. Smith, P. Situ, and W. Volkert, "Evaluation of beta-absorbed fractions in a mouse model for 90y, 188re, 166ho, 149pm, 64cu, and 177lu radionuclides," *Cancer biotherapy & radiopharmaceuticals*, vol. 20, pp. 436–49, 09 2005.

[4] J. Kim and Y. Rahmat-Samii, "Implanted antennas inside a human body: simulations, designs, and characterizations," *IEEE Transactions on Microwave Theory and Techniques*, vol. 52, no. 8, pp. 1934–1943, Aug 2004.

[5] H. Rajagopalan and Y. Rahmat-Samii, "Ingestible rfid bio-capsule tag design for medical monitoring," in *2010 IEEE Antennas and Propagation Society International Symposium*, July 2010, pp. 1–4.

[6] T. Campi, S. Cruciani, F. Palandrani, V. D. Santis, A. Hirata, and M. Feliziani, "Wireless power transfer charging system for aimds and pacemakers," *IEEE Transactions on Microwave Theory and Techniques*, vol. 64, no. 2, pp. 633–642, Feb 2016.

[7] D. Alptekin, "Dual band microstrip implantable antenna design for biomedical applications," Master's thesis, Middle East Technical University, 8 2015.

[8] A. Rosen, M. A. Stuchly, and A. V. Vorst, "Applications of rf/microwaves in medicine," *IEEE Transactions on Microwave Theory and Techniques*, vol. 50, no. 3, pp. 963–974, March 2002.

[9] R. Vetrikani and T. C. Bobby, "Diagnosis of epilepsy — a systematic review," in *2017 Third International Conference on Biosignals, Images and Instrumentation ICBSII*, March 2017, pp. 1–5.

[10] J. L. Stuemke, "Design of a closed loop wireless power transfer system for an electrocorticography device to be implanted in the brain of a rat over an extended period," Master's thesis, University of North Carolina at Charlotte, 2018, copyright - Database copyright ProQuest LLC; ProQuest does not claim copyright in the individual underlying works; Last updated - 2018-06-13. [Online]. Available: https://librarylink.uncc.edu/login?url=https://search.proquest.com/docview/2046325944?accountid=14605

[11] "Ieee standard for safety levels with respect to human exposure to radio frequency electromagnetic fields, 3 khz to 300 ghz," *IEEE Std C95.1-2005 (Revision of IEEE Std C95.1-1991)*, pp. 1–238, April 2006.

[12] I. Acharya, B. Joshi, B. Lanning, and H. Zaveri, "Reconfigurable fault-tolerant multielectrode array for dependable monitoring of the human brain," in *2011 Annual International Conference of the IEEE Engineering in Medicine and Biology Society*, Aug 2011, pp. 652–655.

[13] R. S. Fisher, C. Acevedo, A. Arzimanoglou, A. Bogacz, J. H. Cross, C. E. Elger, J. Engel, L. Forsgren, J. A. French, M. Glynn, D. C. Hesdorffer, B. Lee, G. W. Mathern, S. L. Moshe, E. Perucca, I. E. Scheffer, T. Tomson, M. Watanabe, and S. Wiebe, "Ilae official report: A practical clinical definition of epilepsy," *Epilepsia*, vol. 55, no. 4, pp. 475–482, 2014. [Online]. Available: https://onlinelibrary.wiley.com/doi/abs/10.1111/epi.12550

[14] J. Claassen, S. A. Mayer, R. G. Kowalski, R. G. Emerson, and L. J. Hirsch, "Detection of electrographic seizures with continuous eeg monitoring in critically ill patients," *Neurology*, vol. 62, no. 10, pp. 1743–1748, 2004. [Online]. Available: http://n.neurology.org/content/62/10/1743

[15] R. P. Brenner, "How useful is eeg and eeg monitoring in the acutely ill and how to interpret it?" *Epilepsia*, vol. 50, no. s12, pp. 34–37, 2009. [Online]. Available: https://onlinelibrary.wiley.com/doi/abs/10.1111/j.1528-1167.2009.02350.x

[16] N. Verma, A. Shoeb, J. Bohorquez, J. Dawson, J. Guttag, and A. P. Chandrakasan, "A micro-power eeg acquisition soc with integrated feature extraction processor for a chronic seizure detection system," *IEEE Journal of Solid-State Circuits*, vol. 45, no. 4, pp. 804–816, April 2010.

[17] N. Ida, *Engineering Electromagnetics*, 2nd ed. Springer, 9 2000.

[18] M. Hampe, "Specific absorption rate in human tissues: Accurate and approximated values," in *2013 International Symposium on Electromagnetic Compatibility*, Sept 2013, pp. 143–148.

[19] C. A. Balanis, *Advanced Engineering Electromagnetics*, 2nd ed. John Wiley & Sons, Inc., 2012.

[20] Y. Zhai, M. Yi, S. Li, and S. Xing, "Investigations of specific absorption rate for dual-band pifa antennas," in *2008 8th International Symposium on Antennas, Propagation and EM Theory*, Nov 2008, pp. 323–326.

[21] P. Crespo-Valero, M. Christopoulou, M. Zefferer, A. Christ, P. Achermann, K. S. Nikita, and N. Kuster, "Novel methodology to characterize electromagnetic exposure of the brain," *Physics in Medicine & Biology*, vol. 56, no. 2, p. 383, 2011.

[22] A. Lee, S. Hong, J. Kwon, and H. Choi, "Sar comparison of sam phantom and anatomical head models for a typical bar-type phone model," *IEEE Transactions on Electromagnetic Compatibility*, vol. 57, no. 5, pp. 1281–1284, Oct 2015.

[23] F. Tefiku, "A mobile phone pcs pifa with low sar," in *2007 IEEE Antennas and Propagation Society International Symposium*, June 2007, pp. 4685–4688.

[24] J. Wang, L. Zhao, G. Chen, Y. Wang, and W. Yu, "Ground plane effects on sar for human head model exposed to a dual-band pifa," in *2015 IEEE MTT-S 2015 International Microwave Workshop Series on RF and Wireless Technologies for Biomedical and Healthcare Applications (IMWS-BIO)*, Sep. 2015, pp. 161–162.

[25] C. A. Balanis, *Antenna Theory: Analysis and Design*, 4th ed. Hoboken, NJ, USA: John Wiley & Sons, Inc., 2016.

[26] M. Dich, "Accurate determination of antenna directivity," *IEEE Transactions on Antennas and Propagation*, vol. 45, no. 10, pp. 1502–1505, Oct 1997.

[27] A. K. Skrivervik, J. . Zurcher, O. Staub, and J. R. Mosig, "Pcs antenna design: the challenge of miniaturization," *IEEE Antennas and Propagation Magazine*, vol. 43, no. 4, pp. 12–27, Aug 2001.

[28] L. J. Chu, "Physical limitations of omnidirectional antennas," *Journal of Applied Physics*, vol. 19, no. 12, pp. 1163–1175, 1948.

[29] R. F. Harrington, "Effect of antenna size on gain , bandwidth , and efficiency," 2010.

[30] J. S. McLean, "A re-examination of the fundamental limits on the radiation q of electrically small antennas," *IEEE Transactions on Antennas and Propagation*, vol. 44, no. 5, pp. 672–, May 1996.

[31] S. Gabriel *et al.*, "The dielectric properties of biological tissues: III. parametric models for the dielectric spectrum of tissues," *Physics in Medicine & Biology*, vol. 41, no. 11, pp. 2271–2293, 1996.

[32] K. Foster, "Sh, 1989. dielectric properties of tissues and biological materials: a critical review crc crit," *Rev Biomed Eng*, vol. 17, pp. 25–104, 1989.

[33] P. Debye, *Polar Molecules.* Chemical Catalog Company, Incorporated, 1929. [Online]. Available: https://books.google.com/books?id=eEAwAAAAIAAJ

[34] A. Peyman *et al.*, "Changes in the dielectric properties of rat tissue as a function of age at microwave frequencies," *Physics in Medicine & Biology*, vol. 46, no. 46, pp. 1617–1629, 2001.

[35] W. D. Hurt, "Multiterm debye dispersion relations for permittivity of muscle," *IEEE Transactions on Biomedical Engineering*, vol. BME-32, no. 1, pp. 60–64, Jan 1985.

[36] P. Hall and Y. Hao, *Antennas and Propagation for Body-Centric Wireless Communications, Second Edition*, ser. Artech House antennas and propagation library. Artech House, 2012. [Online]. Available: https://books.google.com/books?id=uufCdhrVlGAC

[37] (accessed 2018) Accuratas cermaic corperation 96% alumina datasheet. [Online]. Available: https://accuratus.com/pdf/96aluminaprops.pdf

[38] (accessed 2018) Durapot potting compound datasheet. [Online]. Available: http://www.cotronics.com/vo/cotr/pdf/801.pdf

[39] Y. Kobayashi and M. Katoh, "Microwave measurement of dielectric properties of low-loss materials by the dielectric rod resonator method," *IEEE Transactions on Microwave Theory and Techniques*, vol. 33, no. 7, pp. 586–592, Jul 1985.

[40] S. il Kwak, K. Chang, and Y. J. Yoon, "Ultra-wide band spiral shaped small antenna for the biomedical telemetry," in *2005 Asia-Pacific Microwave Conference Proceedings*, vol. 1, Dec 2005, pp. 4 pp.–.

[41] V. Shirvante, F. Todeschini, X. Cheng, and Y. Yoon, "Compact spiral antennas for mics band wireless endoscope toward pediatric applications," in *2010 IEEE Antennas and Propagation Society International Symposium*, July 2010, pp. 1–4.

[42] A. Kiourti, M. Christopoulou, S. Koulouridis, and K. Nikita, "Design of a novel miniaturized implantable pifa for biomedical telemetry," vol. 55, 10 2010, pp. 127–134.

[43] W.-C. Liu, S.-H. Chen, and C.-M. Wu, "Bandwidth enhancement and size reduction of an implantable pifa antenna for biotelemetry devices," *Microwave and Optical Technology Letters*, vol. 51, pp. 755 – 757, 03 2009.

[44] Z. D. Liu, P. S. Hall, and D. Wake, "Dual-frequency planar inverted-f antenna," *IEEE Transactions on Antennas and Propagation*, vol. 45, no. 10, pp. 1451–1458, Oct 1997.

[45] A. A. Roy, J. M. MÃŽm, and D. T. Kureve, "Effect of dielectric constant on the design of rectangular microstrip antenna," in *2013 IEEE International Conference on Emerging Sustainable Technologies for Power ICT in a Developing Society (NIGERCON)*, Nov 2013, pp. 111–115.

[46] K. Wong, *Planar Antennas for Wireless Communications*, ser. Wiley Series in Microwave and Optical Engineering. Wiley, 2003. [Online]. Available: https://books.google.com/books?id=wnOBQgAACAAJ

[47] H. T. Chattha, Y. Huang, X. Zhu, and Y. Lu, "An empirical equation for predicting the resonant frequency of planar inverted-f antennas," *IEEE Antennas and Wireless Propagation Letters*, vol. 8, pp. 856–860, 2009.

[48] K. Ogawa and T. Uwano, "A diversity antenna for very small 800-mhz band portable telephones," *IEEE Transactions on Antennas and Propagation*, vol. 42, no. 9, pp. 1342–1345, Sep. 1994.

[49] L. H. Mei, S. S. Ming, Z. Hua, and L. X. Bo, "The effect of slots on pifa performance," in *2015 IEEE 4th Asia-Pacific Conference on Antennas and Propagation (APCAP)*, June 2015, pp. 485–487.

[50] H. Wang and M. Zheng, "Input impedance-tuning slots of pifa antennas," in *The Second European Conference on Antennas and Propagation, EuCAP 2007*, Nov 2007, pp. 1–4.

[51] J.-S. Row, C.-H. Hsu, and C.-Y. Ai, "Studies of the planar inverted-f antenna with a u-shaped slot," in *IEEE Antennas and Propagation Society International Symposium. Digest. Held in conjunction with: USNC/CNC/URSI North American Radio Sci. Meeting (Cat. No.03CH37450)*, vol. 2, June 2003, pp. 561–564 vol.2.

[52] P. Salonen, M. Keskilammi, and M. Kivikoski, "Single-feed dual-band planar inverted-f antenna with u-shaped slot," *IEEE Transactions on Antennas and Propagation*, vol. 48, pp. 1262–1264, 08 2000.

[53] ——, "Dual-band and wide-band pifa with u- and meanderline-shaped slots," in *IEEE Antennas and Propagation Society International Symposium. 2001 Digest. Held in conjunction with: USNC/URSI National Radio Science Meeting (Cat. No.01CH37229)*, vol. 2, July 2001, pp. 116–119 vol.2.

[54] Y. Jean-Charles, V. Ungvichian, and J. A. Barbosa, "Effects of substrate permittivity on planar inverted-f antenna performances," *Journal of Computers*, vol. 4, no. 7, pp. 610–614, July 2009.

[55] F. Tavakkol-Hamedani, L. Shafai, and G. Z. Rafi, "The effects of substrate and ground plane size on the performance of finite rectangular microstrip antennas," in *IEEE Antennas and Propagation Society International Symposium (IEEE Cat. No.02CH37313)*, vol. 1, June 2002, pp. 778–781 vol.1.

[56] N. A. Islam and F. Arifin, "Performance analysis of a miniaturized implantable pifa antenna for wban at ism band," in *2016 3rd International Conference on Electrical Engineering and Information Communication Technology (ICEEICT)*, Sep. 2016, pp. 1–5.

[57] S. Sultana, R. R. Hasan, T. K. Mondal, R. T. H. Tusher, and S. Zabin, "Performance analysis of body implantable pifa at different substrate material," in *2017 4th International Conference on Advances in Electrical Engineering (ICAEE)*, Sep. 2017, pp. 68–73.

[58] D. Alptekin, L. Alatan, and N. G. GenÃ§er, "Dual band pifa design for biomedical applications," in *2016 10th European Conference on Antennas and Propagation (EuCAP)*, April 2016, pp. 1–4.

[59] S. Sultana, M. M. Miran, S. M. A. Uddin, M. M. Naby, and M. Haque, "Performance analysis of a modified implantable pifa operates at mics band for human head phantom model," in *2017 3rd International Conference on Electrical Information and Communication Technology (EICT)*, Dec 2017, pp. 1–5.

[60] A. Bashkatov, E. Genina, I. V. Korovina, Y. P. Sinichkin, O. V. Novikova, and V. Tuchin, "In-vivo and in-vitro study of control of rat skin optical properties by action of 40%-glucose solution," *Proceedings of SPIE - The International Society for Optical Engineering*, vol. 4241, 05 2001.

[61] H. Takeuchi, M. Ishida, A. Furuya, H. Todo, H. Urano, and K. Sugibayashi, "Influence of skin thickness on the <i>in vitro</i> permeabilities of drugs through sprague-dawley rat or yucatan micropig skin," *Biological and Pharmaceutical Bulletin*, vol. 35, no. 2, pp. 192–202, 2012.

[62] M. A. O'Reilly, A. Muller, and K. Hynynen, "Ultrasound insertion loss of rat parietal bone appears to be proportional to animal mass at submegahertz," *Ultrasound in medicine & biology*, vol. 37, pp. 1930–1937, 09 2011.

[63] H. P. Zaveri, L. D. Iasemidis, W. J. Williams, and J. C. Sackellares, "Multielectrode analysis of the electrocorticogram in temporal lobe epilepsy," in *Proceedings of the Annual International Conference of the IEEE Engineering in Medicine and Biology Society*, Nov 1988, pp. 1198–1200 vol.3.

[64] M. A. Sayeed, S. P. Mohanty, E. Kougianos, and H. Zaveri, "An energy efficient epileptic seizure detector," in *2018 IEEE International Conference on Consumer Electronics (ICCE)*, Jan 2018, pp. 1–4.

[65] (accessed 2018) Rhd2132 faq: Amplifier gain. [Online]. Available: http://intantech.com/files/Intan_RHD2000_series_gain_FAQ.pdf

APPENDIX A: FIELD COMPONENTS OF CAVITY MODES

Using (4.9) and (4.21) the rest of the field components may be expressed as

$$E_x = \frac{\beta_y}{\varepsilon} A_{mnp} cos(\beta_x x) sin(\beta_y y) sin(\beta_z z) \tag{A.1}$$

$$E_y = -\frac{\beta_x}{\varepsilon} A_{mnp} sin(\beta_x x) cos(\beta_y y) sin(\beta_z z) \tag{A.2}$$

$$E_z = 0 \tag{A.3}$$

$$H_x = j\frac{\beta_x \beta_y}{\omega\mu\varepsilon} A_{mnp} sin(\beta_x x) cos(\beta_y y) cos(\beta_z z) \tag{A.4}$$

$$H_y = j\frac{\beta_y \beta_z}{\omega\mu\varepsilon} A_{mnp} cos(\beta_x x) sin(\beta_y y) cos(\beta_z z) \tag{A.5}$$

$$H_z = -j\frac{A_{mnp}}{\omega\mu\varepsilon}(-\beta_z^2 + \beta^2) cos(\beta_x x) cos(\beta_y y) sin(\beta_z z) \tag{A.6}$$

APPENDIX B: BOM FOR SCHEMATIC OF COMMUNICATION SYSTEM

Reference	**Package**	**Value**
R1	0402	0Ω
R2	0402	56kΩ
C1	0402	18pF
C2	0402	18pF
C3	0402	1pF
C4	0402	1pF
C5	0402	1pF
C6	0402	1μF
C7	0402	12pF
C8	0402	12pF
C9	0402	100nF
C10	0402	100nF
C11	0402	100nF
C12	0402	100nF
C13	0402	100nF
C14	0402	100nF
C15	0402	100nF
C16	0402	100nF
L1	0402	2nH

L2	0402	2nH
L3	0402	1nH
L4	0402	3nH
Q1	FA-128	32MHz crystal
U1	QFN 32pin	CC2543
U2	QFN 56pin	RHD2132

Table B.1: Bill of materials for the schematic in figure 6.4.